Impact of climate change on the production and transport of sea salt aerosol on European seas

J. Soares[1], M. Sofiev[1], C.Geels[2], J.H.Christensen[2], C.Andersson[3], S. Tsyro[4], J.Langner[3]

[1] Finnish Meteorological Institute, Helsinki, Finland

[2] Department of Environmental Science, Aarhus University, Roskilde, Denmark

[3] Swedish Meteorological and Hydrological Institute, Norrköping, Sweden

[4] EMEP MSC-W, Norwegian Meteorological Institute, Oslo, Norway

Correspondence to: J. Soares (joana.soares@fmil.fi)

Abstract

The impact of climate change on sea salt aerosol production, dispersion, and fate over Europe is studied using four offline regional chemistry transport models driven by the climate scenario SRES A1B over two periods: 1990-2009 and 2040-2059. The study is focused mainly on European seas: Baltic, Black, North and Mediterranean. The differences and similarities between predictions of the individual models on the impact on sea salt emission, concentration and deposition due to changes in wind gusts and seawater temperature are analysed. The results show that the major driver for the sea-salt flux changes will be the seawater temperature, as wind speed is projected to stay nearly the same. There are, however, substantial differences between the model predictions and their sensitivity to changing seawater temperature, which demonstrates substantial lack of current understanding of the sea-salt flux predictions. Although seawater salinity changes are not evaluated in this study, sensitivity of sea-salt aerosol production to salinity is similarly analysed, showing once more the differences between the different models. An assessment on the impact of SSA to the radiative balance is presented.

1 Introduction

The sea-salt aerosol (SSA) affects the Earth radiation budget, atmospheric chemistry, cloud processes, and climate (O'Dowd et al., 1997; IPCC, 2013). Anthropogenic and natural aerosols have similar annual impacts on the global radiative balance, though being predominant in different locations (Textor et al., 2006). SSA dominates the particulate mass and it is the major contributor to aerosol optical depth (AOD) over the ocean (Quinn et al, 1998).

SSA originates from sea spray droplets resulting from waves breaking on the seawater surface, forming whitecaps that cause the entrainment of air into the water. The two main mechanisms responsible for sea spray formation are air bubble bursting during whitecap formation and decay, and direct tearing of droplets from the top of breaking waves. Therefore, the formation of primary SSA is mainly dependent on wind speed: the emission of SSA is generally considered to be proportional to surface winds cubed (Monahan et al., 1986), suggesting that small changes in surface winds can have a substantial impact on the emission of this natural aerosol. Further on, studies on the marine aerosol size distribution (e.g. Covert et al., 1998; Russell and Heintzenberg, 2000; Bates et al., 2002; Huebert et al., 2003) suggest that for high wind speeds the production of very coarse SSA (with particle diameter (Dp) > 20 mm) increases, contributing to a higher transfer of heat and water vapour from the ocean to the atmosphere (Andreas et al., 1995). These processes have a strong impact on the climate forcing. Other parameters influencing the formation of primary SSA have been identified, e.g., seawater temperature and salinity, atmospheric stability, and wave height and steepness (O'Dowd and Smith, 1993; Gong et al., 1997; Gong, 2003; Mårtensson et al., 2003; Lewis and Schwartz, 2004; O'Dowd and de Leeuw, 2007; Witek et al., 2007a, 2007b; Ovadnevaite et al., 2014). Laboratory studies by Mårtensson et al. (2003) and in situ measurements by Nilsson et al. (2007) show that for nano-sized particles, the aerosol number emission decrease with increasing seawater temperature, and for particles with Dp > 100 nm, the number SSA increase with increasing seawater temperature; reflecting different sea spray formation processes. Seawater salinity also affects the droplet formation, where formation of particles with Dp < 0.2 μm are not affected by salinity, but for larger Dp's, salinity impact is substantial: higher salinity contributes to higher production (Mårtensson et al., 2003). The SSA removal processes are scavenging by precipitation and dry deposition (including gravitational settling). SSA has an effect on secondary aerosols formed by gas-to-particulate conversion process such as condensation and nucleation (binary homogeneous and heterogeneous) (Twomey, 1997). SSA serves as a sink for condensable gases and smaller aerosol particles, and serves also as a medium for aqueous-phase reaction of

reactive gases, e.g. H_2SO_4. This can lead to nucleation suppression for other components of the marine aerosol and consequently change their size distribution, creating a feedback on climate. Furthermore, SSA formation results in a size spectrum ranging from 0.01 to 100 µm, which can lead to cloud formation. With increasing concentrations of cloud condensation nuclei (CCN), the cloud microphysical properties change, i.e., the available water vapour is re-distributed over more particles, on average resulting in smaller particle sizes, which in turn changes both cloud albedo and precipitation (Latham et al., 2008, Lenton and Vaughan, 2009; Boyd, 2008; Korhonen et al., 2010, Wang et al., 2011). With dry diameter lower than 1 µm, SSA can easily be transported for long distances in the atmosphere, serving as a cloud seed outside of heavily clouded regions. The cloud drop number concentration can be spatially different, depending on the wind speed, atmospheric transport and particle loss via dry and wet deposition (Korhonen et al., 2010).

Changes in atmospheric transport pathways, precipitation patterns, and sea ice cover influence transport, removal and distribution of SSA. The main features of the regional and global SSA distribution and the climate impact on SSA production due to these physical drivers have been discussed in studies such as Liao et al. (2006), Pierce and Adams (2006), Manders et al. (2010), Sofiev et al. (2011), Struthers et al. (2011), and Tsyro et al. (2011). The understanding of sea spray emissions has increased substantially but process-based estimates of the total mass and size distribution of emitted sea spray particles continue to have large uncertainties (de Leeuw et al., 2011). Chemical transport models (CTM) and general circulation models (GCM) estimates of sea salt burden may vary over 2 orders of magnitude (Textor et al., 2006) and climate models disagree about the balance of effects, ranging from little (Mahowald et al., 2006a) to a considerable sensitivity to climate change (Bellouin et al., 2011). The difference between the available estimations might be due to the wind speed predicted by the climate models, with little understanding of how wind speed may change over the ocean in a warmer climate (IPCC, 2013).

The main goals of the current study are to assess the sensitivity of the production, surface concentrations and removal of SSA to climate change. A multi-model approach using four state-of-the-art offline CTMs was taken to assess the uncertainty/robustness of model predictions over Europe. The sensitivity of simulated emission, concentration, and deposition of SSA to changes in climate was evaluated by comparing a past (1990-2009) and a future (2040-2049) period. This study is a follow-up to the climates studies of Langner et al. (2012) focusing on surface ozone and Simpson et al. (2014) focusing on nitrogen deposition.

2 Methods

This study uses the same modelling structure as in Langner et al. (2012) for ozone and in Simpson et al (2014) for nitrogen. We focus on the comparison of SSA simulations from three offline European-scale CTMs - EMEP MSC-W, MATCH and SILAM - and one offline hemispheric CTM, DEHM. The models were run through a past (1990-2009) and a future (2040-2059) climate scenarios and the results for the European seas (Baltic, North, Mediterranean, and Black Seas) were compared. The climate meteorology data from a GCM were used in a regional climate model (RCM) and the hemispheric model DEHM. The regional models where driven by the downscaled meteorology from the RCM and the boundary conditions from DEHM. The horizontal grid for DEHM is 150x150 km^2 and for the regional CTMs identical to the RCM (ca. 50×50 km^2).

Throughout the paper, the SSA mass refers to the total mass of dry particles. Since the observations measure sodium (Na^+) concentrations rather than total SSA mass, it is assumed that Na^+ mass fraction is ~30% (Seinfeld and Pandis, 2006). Particle sizes are also provided for dry conditions and, unless otherwise stated, the dry diameter D_p ranges up to 10 μm.

2.1 Climate meteorology

Results of the global ECHAM5/MPIOM GCM (Roeckner et al., 2006), driven by emissions from the SRES A1B scenario (Nakicenovic, 2000), were downscaled over Europe with the Rossby Centre Regional Climate model, version 3 (RCA3) (Samuelsson et al., 2011; Kjellstrom et al., 2011). The global ECHAM5/MPIOM model is defined in spectral grid T63, which at mid-latitudes corresponds to a horizontal resolution of ca. 140×210 km^2. The horizontal resolution of RCA3 was 0.44º×0.44º on a rotated latitude-longitude grid, and data were provided with 6-hourly resolution. The climate, as downscaled by RCA3, reflects the broad features simulated by the parent GCM, but from earlier studies with the current setup it is clear that the global ECHAM5/MPIOM model projects a slightly warmer and wetter climate over Europe than the regional model RCA3 (Langner et al., 2012; Simpson et al., 2014).

The wind speed is higher over the ocean and can be up to two times slower, on average, over the inner seas (Fig. 1, first panel on the left). Wind patterns are different between the Seas, with some areas over individual seas being more affected by wind gusts than others: e.g. in the Mediterranean, the wind speed is higher over the Levantine Sea than over other areas. For the wind speed, RCA3 predicts a stronger increase at the Norwegian Sea, Black Sea, Gulf of Bothnia (Baltic Sea) and Aegean Sea (Mediterranean Sea) and a stronger decrease between Italy and Tunisia and Libya

(Mediterranean Sea) in the future period (Fig. 1, first panel on the right). Nevertheless, the absolute change is no more than 0.4 m/s. Trend analysis considering only marine grid cells for each sea (Fig. S1 in supplementary material) shows that there is no significant trend between past and future periods.

Typically, the surface water temperature is higher at southern latitudes. For the same latitude, the Black and Mediterranean Seas have, in general, higher temperature than the Atlantic Ocean and the Baltic Sea (Fig. 1, second panel on the left). RCA3 predicts a general increase of the water surface temperature between the past and the future periods (Fig. 1, second panel on the left). The most substantial changes are for the northern part of the Atlantic Ocean and for the Baltic Sea (maximum 1.17 ºC). Trend analysis for the monthly mean temperature is significant for all the European inner-seas (Fig. S2 in supplementary material). The temperature is rising for all the seas with the highest rise over the Black Sea and the lowest over the North Sea.

The precipitation tends to be higher over the ocean and lower over the inner seas. The lowest precipitation amount is seen over the Mediterranean Sea; on an annual level the difference from the ocean can be up-to two orders of magnitude (Fig. 1, third panel on the left). The climate model predicts that the precipitation will strongly decrease over the Mediterranean and increase over the Baltic and North Seas, whereas over different parts of Atlantic Ocean the opposite trends can coexist (Fig. 1, third panel on the right). Trend analysis shows that none of the trends is significant (Fig. S3 in supplementary material).

2.2 SSA boundary conditions

Sea salt concentrations (as fine and coarse modes, see the description of DEHM below) provided by the hemispheric DEHM model, were used as lateral and top boundaries for the regional models. The boundary values taken from DEHM were updated every 6 h and interpolated from the DEHM grid to the respective geometry of each regional CTM. The DEHM model was driven by the global ECHAM5-r3 meteorology, without the RCA-3 downscaling.

2.3 Chemical transport models

The models used in this study have been introduced in the previous studies: Langner et al. (2012) and Simpson et al. (2014). Below, we focus on their handling of the production and removal of SSA. All the SSA source functions in the current study are based on the SSA production via bubble-mediated mechanism, taking into account the effects of wind speed and seawater properties.

Mårtensson et al. (2003) parameterization is taken for the sub-micron aerosols and white-cap-area based parameterizations of Monahan et al. (1986) are used for formation of super-micron particles. These parameterisations are described in supplementary material Eq. S1 and Eq. S2. The sea salt flux estimation assumes a constant relative humidity of 80% for DEHM and EMEP, while in MATCH and SILAM the relative humidity was predicted by RCA-3. The difference between the various source functions is the dependence on temperature and salinity for the SSA generation (Table 1).

2.3.1 DEHM

In DEHM the production of SSA at the ocean surface is based on two parameterization schemes describing the bubble-mediated sea spray production of smaller and larger aerosols. In each time step the production is calculated for seven size bins and thereafter summed up to give an aggregated production of fine (with dry diameters <1.3 μm) and coarse (with dry diameters ranging 1.3-6 μm) aerosols (using a density of 2200 kg m^{-3}), assuming a log-normal distribution within the modes when calculating the emission. For the fraction with dry diameters less than 1.25 μm a source function based on Mårtensson et al. (2003) is used, while for sizes larger than that the Monahan et al. (1986) source function is applied. They both include an $U_{10}^{3.41}$ dependency on wind speed and the production of the smaller aerosols is also a function of the sea surface temperature. An ambient relative humidity of 80% is assumed in the calculations and the size of the produced SSA is assumed to depend on the salinity at the actual location. Here a monthly climatology of current day salinity on a 0.25°x0.25° grid (Boyer et al., 2005) is applied for both time periods in focus in the current paper. Within the atmosphere, the fine and coarse fraction of SSA is treated separately in terms of transport and removal. Wet deposition includes in-cloud and below-cloud scavenging, while dry deposition velocities are based on typical resistance methods for various land surface types (see Simpson et al., 2003; Emberson et al., 2000). The fine and coarse fractions in the DEHM model are in the current paper assigned the dry diameters of 1 μm and 6 μm.

DEHM is continuously validated against available measurements from e.g. the EMEP network and an evaluation of an earlier version of the sea salt routine in DEHM showed that the model gives satisfactory results for sea salt over Europe (Brandt et al. 2012).

2.3.2 EMEP MSC-W

The standard Unified EMEP model runs include sea salt particles with ambient diameters up to about 10 μm, which mainly originate from the bubble mediated sea spray (Tsyro et al, 2011). The

parameterisation scheme for calculating sea salt generation in the EMEP model makes use of two source functions for bubble-mediated sea spray production. The first one is a source function for sea spray droplets at 80% relative humidity from Monahan et al. (1986) and the second one is a source function for sea salt particles from the work of Mårtensson et al. (2003), which is formulated for a salinity of 33‰. In the EMEP model, the SSA fluxes can be calculated for particle dry Dp ranging from 0.02 to 12 μm, whereas operationally and for this work SSA with Dp up to 6 μm are included. When calculating the emission, EMEP assumes a log-normal distribution; the bins within fine and coarse fractions are integrated and then advect as fine and coarse sea salt mass (no size distribution). Mårtensson et al. (2003) parameterisation is applied for smaller size bins, while Monahan et al. (1986) parameterisation is used for the coarser ones. From the fluxes of sea spray, the sea salt mass is calculated assuming sea salt density of 2200 kg m^{-3}. The total production rates of fine and coarse sea salt are calculated by integrating the size resolved fluxes (7 in the fine and 3 in the coarse fractions) over respective size intervals. In the model, generated SSA is assumed to be instantaneously mixed within the model lowest layer at each time step. The transport and removal of sea salt is described individually for the fine and coarse fractions in the EMEP model. Dry deposition parameterisation for aerosols is calculated using a mass-conservative equation from Venkatram and Pleim (1999). The dry deposition due to gravitational settling is size-dependent and diameters of 0.33 and 4.8 μm are assumed for the fine and coarse SSA. Wet scavenging is treated with simple scavenging ratios, accounting for in-cloud and sub-cloud processes. The scavenging ratios are assigned to crudely reflect the solubility of different aerosol components, and the size differentiated collection efficiencies are used in sub-cloud aerosol washout.

The present sea salt parameterisation was shown to give the best overall results as compared to a number of other source functions within the EMEP model (Tsyro et al., 2011). The model SSA calculations are extensively evaluated against long-term observations (Tsyro et al., 2011; EMEP Reports http://www.emep.int).

2.3.3 MATCH

The treatment of SSA production in MATCH is based on the parameterization of Mårtensson et al. (2003) for dry particle sizes of up to 0.4 μm aerodynamic radius, and on Monahan et al. (1986) for larger particle sizes. The temperature correction following Sofiev et al. (2011) is applied to the estimates from the Monahan scheme. The number of bins is flexible, but in this study four size bins were used with Dp ranges 0.02–0.1 μm, 0.1–1 μm, 1–2.5 μm, 2.5–10 μm, assuming a log-normal distribution within the modes when calculating the emission. The production of sea salt droplets is

calculated assuming a dynamic relative humidity and a particle density of 2170 kg m^{-3} and is integrated over each size bin while dry removal rates are calculated using the geometric mean size in each bin. Dry deposition over land is following Zhang et al. (2001) while a separate parameterization accounting for bubble burst activity is used over sea (Pryor and Barthelmie, 2000). Sea salt is assumed to 100% activated or scavenged by hydrometeors in-cloud while below-cloud scavenging is handled following Dana and Hales (1976). The distribution of salinity (on 1°x1°) in sea water is taken from NOAA (2013). Further details and evaluation of MATCH sea salt simulations using observed meteorology can be found in Foltescu et al. (2005) and Andersson et al. (2015).

2.3.4 SILAM

The SSA takes into account the effects of wind speed, salinity and water temperature and covers sea salt particles with dry diameter from 20 nm to 10 μm. The observations from the Mårtensson et al. (2003) study for seawater surface temperature 298 K and sea water salinity 33 ‰ were used to extrapolate the scheme from Monahan et al. (1986) to particle sizes down to 20 nm. To calculate SSA production for other water temperatures and salinities, correction factors are applied which were derived based on the experimental data of Mårtensson et al. (2003). The full description of the parameterisation in the SILAM model can be found in Sofiev et al. (2011). The description of the temperature correction in Sofiev et al. (2011) was changed. Currently, the water temperature reference for the unified shape function is 20 ºC, instead of 25 ºC as referred in Sofiev et al. (2011). The shape function has been updated accordingly and the new shape function (dF_0/dD_p) for particles with Dp ranging from 0.01 to 10 μm is described below:

$$\frac{dF_0}{dD_p} = (1 + 0.05 * D_p) * \frac{\exp\left(\frac{-0.11}{D_p}\right)}{0.4 + \exp\left(\frac{-0.2}{D_p}\right)} * \frac{6 * 10^5}{\left(1 * 10^{-4} * D_p^2 + D_p\right)^3} * 10^{1.19 * \exp\left(-\left(\frac{0.35 - \lg D_p}{0.8}\right)^2\right)} \quad (1)$$

For the current study the spume droplet formation based on Andreas (1998) was included, with spume being supressed for 10m wind speed lower than 6 m/s. The production of sea salt droplets is calculated assuming a dry particle density of 2200 kg/m^3. The size distribution is described by flexible bins. Production is integrated over each size bin while dry and wet removal rates are calculated using mass-weighted mean diameter in each bin. Depending on particle size, mechanisms of dry deposition vary from primarily turbulent diffusion driven removal of fine aerosols to

primarily gravitational settling of coarse particles (Kouznetsov and Sofiev, 2012). Wet deposition distinguishes between sub- and in-cloud scavenging by both rain and snow (Sofiev et al., 2006; Horn et al., 1987; Smith and Clark, 1989; Jylhä, 1991). Gravitational settling, dry deposition and optical properties take into account the particle hygroscopic growth. For the simulations, five bins with the Dp ranges of 0.01–0.1 μm, 0.1–1.5 μm, 1.5–6 μm, 6–15 μm; and 15-30 μm, assuming a log-normal distribution within the modes when calculating the emission. The distribution of salinity in sea water is taken from NOAA (2013).

SILAM model has been evaluated against a wide range of observations and models utilizing the above described parameterization (Sofiev et al., 2011; Tsyro et al., 2011).

2.4 Model evaluation

Sea water is the predominant source of Na^+ in the atmosphere, which can be used as its tracer in most regions of Europe. Evaluation of the model predictions was performed via comparison with observations available from the EMEP network (Co-operative Programme for monitoring and evaluation of the long-range transmission of air pollutants in Europe, http://www.emep.int, Tørseth et al. 2012) that perform regular measurements across Europe. The observations include Na^+ concentration in aerosol and ion analysis of precipitation including Na^+. Concentration measurements are sampled daily by a filter pack sampler (cut-off at D_p = ~10 μm), at 2 m height; the concentration in precipitation is mainly sampled by a "wet-only" sampler and, in a few places, with bulk collectors. The wet deposition of Na^+ is obtained by multiplying the weighted mean concentration by the total amount of precipitation on a daily basis. For more details about the sampling the reader is referred to e.g., Hjellbrekke and Fjæra (2009). These sampling methods do not distinguish if the sodium is originated from natural (e.g. mineral dust) or anthropogenic sources. In some regions there might be certain amounts coming from combustion processes and industry, but overall the contribution of anthropogenic sources to the sodium budget is low (van Loon et al., 2005).

The measurement data were averaged to monthly level with the minimum completeness requirement of 75% temporal coverage per month and per year, between 1990 and 2009. The CTMs predictions for the measurement sites satisfying the temporal criterion were averaged on a monthly basis over the 20 years. Since the model computations were driven by climate model fields, no temporal collocation was done. Therefore, the primary parameter considered was the monthly Na^+ concentrations averaged over the past period. Modelled values were obtained from the model's

lowest layer mid-point, which is defined somewhat differently for each model (Table 1). No near-surface concentration profiling was made, with the exception of EMEP where concentrations are corrected to 3 m height, largely due to unreliable stability estimates based on climate-model fields.

The model performance was evaluated by the following statistical measures: bias, spatial Pearson correlation coefficient (R), root mean square error (RMSE), bias and standard deviation (SD) ratio ($SD_{model}/SD_{observations}$). The evaluation included Na^+ concentration in aerosols at 29 measurement sites and ion analysis of Na^+ wet deposition at 133 measurement sites, which we consider sufficient for computing the basic statistical scores and plotting scatter plots. The location of the measurement sites are shown in Fig. S4 in the supplementary material.

2.5 Radiative transfer modelling

The radiative transfer modelling was completed offline with the libRadtran software package for radiative transfer calculations (Mayer and Kylling, 2005). This tool calculates radiances, irradiances and actinic fluxes for the given optical properties. The Earth radiative balance results from the difference between the incoming (direct and diffusive-downwards) and outgoing (diffusive upwards) radiation. The impact of SSA is assessed by the difference between an atmosphere with SSA and without SSA, for the past and future periods. The calculations were defined at the top of the atmosphere (TOA), with wavelength ranging from 0.2 to ~4 μm, in order to compute the integrated shortwave irradiance. All the runs considered wet and icy clouds, with the cloud cover taken from the climate model RCA3 and optical properties taken from MODIS observations (Pincus et al. 2011). Monthly-basis observations from AQUA and TERRA obtained from 2002 to 2014 were averaged in order to have climatological cloud optical fields. These fields were the same for both past and future period calculations. Earth albedo information is included in the calculations and is obtained from the NASA model, GLDAS Noah Land Surface Model L4 (Rodell et al., 2004), on a monthly basis for the period between 1990 and 2012. This dataset was averaged to obtain climatological surface albedo fields, remaining the same for both past and future periods. The aerosol optical properties of SSA were specified to define profiles of optical thickness, single scattering albedo and asymmetry factor. The optical thickness profile for an atmosphere with SSA was computed by SILAM. SILAM's optical thickness predictions for 500 nm wavelength were computed based on the size distribution described in Table 1 and spectral refractive index of SSA (Prank, 2008). The AOD data was monthly-averaged for every hour in a day, for the past and future periods. This allowed taking into consideration the length of the day, since solar zenith angle is

computed for every hour. The description of the runs and assumptions are provided in Table 2. This setting was chosen in order to reflect an atmospheric state closer to reality, since there were no other aerosols available for this study. Keeping the atmospheric and cloud conditions constant between the past and the future, will allow pinpointing the impact of the SSA on the radiative balance.

3 Results

3.1 Comparison with observations

Table 3 and Table 4 show the performance of the CTMs in estimating Na^+ surface concentrations and wet deposition, respectively, during the past period. The models showed similar performance with quite high correlation coefficients varying from 0.71 up to 0.85 for the concentrations but substantially lower for wet deposition (from 0.24 up to 0.41). The difference between the model performances is quite small and varying for the different scores. The highest correlation coefficient with the concentration observations was shown by DEHM (0.85), which also demonstrated the highest RMSE and bias originating from a stronger overestimation over the regions with observed low concentrations. EMEP showed the lowest RMSE and bias, as well as one of the best correlation factors. SILAM tends to overestimate the lowest observed values (positive bias) whereas MATCH has a stronger underestimation of the highest values (negative bias). Comparing the winter (December, January and February) and the summer (June, July and August) seasons, one can notice that the models perform better in summer, with higher correlation and lower bias. The observed winter time levels are likely harder to be reproduced due to stronger winds and faster changing weather, which might not be captured by the climatological runs.

Comparison of Na^+ wet deposition with measurements shows low correlation and substantial under-prediction. This is particularly true for the high-deposition observations, which resulted in a strong negative bias for all the models. The evaluation of modelled precipitation was presented in Simpson et al. (2014), Table 4, and shows an overestimation of precipitation in the RCA3 model (regional CTMs) and underestimation in the precipitation used in DEHM. The overestimation leads to an overestimation of the deposition of SSA close to the sources. Consequently, less SSA reaches the shore and the measurement sites. The second major reason for discrepancy is that the observed wet deposition does not cut-off the size of the particles, i.e. SSA coarser than 10 μm is accounted for, including the SSA produced in the surf zone. This mostly explains the large negative bias of the models, which reported PM_{10} only, and, to some extent, the low correlation. This is demonstrated when comparing SILAM scores taking into account the full size range available (Dp = [0.01-30]

μm): accounting for the coarser aerosols strongly reduced the bias, correlation strongly improved, and RMSE became slightly smaller. In summer, the scores are slightly better than in winter, but the absolute values and importance of this removal process is smaller in summer time.

In Simpson et al. (2014), it was shown that CTMs driven by RCM meteorology are likely to perform worse than they would with data from numerical weather prediction models. Nevertheless, the current comparison showed that CTMs can predict mean concentrations and depositions within ~30% uncertainty (for depositions, prediction of full size range is a pre-requisite), whereas the spatial distribution patterns are reproduced with correlation higher than 0.7 also when driven by climate model meteorology.

3.2 Current and future climate SSA emissions

The annual SSA emission in the reference period predicted by DEHM, MATCH and SILAM is shown in Figure 2 (left panel). EMEP did not include this variable as an output. As expected, all models predict the highest emissions over the Atlantic Ocean, with the Mediterranean Sea being the second highest source. MATCH predicted, on average, 25% higher emissions over the Mediterranean than SILAM. The emissions are mainly driven by the wind and typically expressed by the white-cap produced by the surface-winds via the Monahan and O'Muircheartaigh (1980) parameterisation. This empirical power-law is taken by all models participating in this study and suggests emission (E) to be proportional to the 10m-wind speed (U_{10}) to the power of 3.41: $E \approx U_{10}^{3.41}$, the so-called wind-forcing. Consequently, the SSA emissions (Fig. 2, left panel) clearly correlate with the wind-forcing (Figure 3, left panel), in particular over the open ocean. However, the use of the same functional dependence and input meteorology does not guarantee identical emission, as it will be discussed further on. MATCH and SILAM seem more sensitive to the wind-forcing over the Mediterranean than DEHM, possibly due to the horizontal resolution difference between the hemispheric and regional CTMs (e.g. the Mediterranean is not properly resolved by the global climate model, the driver for DEHM). Apart from the wind forcing, laboratory studies have shown the relation between the emissions of SSA and seawater surface temperature and salinity: SSA mass will be higher at sea areas with higher surface water temperatures and salinity (Mårtensson et al, 2003). The temperature and salinity dependencies are included in the parameterizations, therefore, the models predict for the same wind forcing, higher emissions for higher water temperatures: the Mediterranean and Black Seas (Fig. 1 and Fig.2, left panel). The effect of salinity is best seen in the Baltic Sea (salinity ~ 9 ‰), which has comparable wind forcing

to some areas of the Mediterranean and the Atlantic (salinity ~33 ‰) but lower emission. SILAM and MATCH show the highest difference between the inner-seas with at least 3 times lower emissions over the Baltic Sea.

In absolute terms, the climate impact on SSA emissions (Fig. 2, right panel) is mainly positive according to the regional models whereas DEHM shows a general decrease. The exception goes for the Atlantic Ocean, in the west side of the domain, where all the models agree in a decrease of emissions. The difference between the past and future periods is only due to the wind forcing and temperature changes, since salinity was kept constant. Thus, this change (Fig. 2, right panel) highly correlates with the changes for wind-forcing (Fig. 3, right panel), adjusted by the changes in water temperature (Fig. 1, right panel). For example, the pronounced decrease of emission over western Atlantic is mainly driven by the reduction of wind speed but the decrease is limited by the rising temperature in the north and east: higher temperature leads to production of more SSA even for somewhat slower wind speed.

The models demonstrated different sensitivity to seawater temperature: it seems to be less important for DEHM than for other models, whereas SILAM is the most sensitive. For instance, MATCH and SILAM showed an increase of emissions over the east of Iceland where temperature is predicted to rise by almost 2 K. The increase of seawater temperature, supported by higher wind speed, over the Black and Aegean Seas (Fig. 1, right panel), will lead to higher emissions. DEHM might not be so sensitive to the local storms due to the coarse horizontal resolution. The absolute difference between future and past is the smallest for the Baltic Sea, but in relative terms all the models show an increase up to 20% in Gulf of Bothnia, which is actually higher than, e.g. 5-15% of increase predicted for North Sea (minimum for DEHM and maximum for MATCH).

Trend analysis for the Baltic, Black, Mediterranean and North Seas (only sea cells are taken into consideration) is available as supplementary material: Fig. S5 for the Baltic, Fig. S6 for the Black, Fig. S7 for the Mediterranean, and Fig. S8 for the North Seas. The trend is only statistically significant ($p < 0.001$) for all the models for the Black Sea, with all models agreeing on an increase of concentration in the future.

Figure 4 (left panel) shows the SSA emission difference between the winter and summer for the past period. The difference between seasons in terms of SSA production can be substantial: SSA emission is up to 3 times higher in winter time. Seasonally, there are differences between the driving processes for SSA production: the winter period has a larger SSA production, due to more frequent and stronger storms; but the summer time shows pronounced maxima over specific areas

mostly influenced by the seawater temperature. The latter is mostly true for MATCH and SILAM, since their temperature sensitivity is higher. SSA emission in winter will be accentuated in the future for MATCH (more emphasized) and SILAM: Figure 4 (right panel) shows pronounced maxima around Iceland and the British Isles; distinct differences in the SSA emission are also seen in the Mediterranean. DEHM does not show much difference between the periods.

3.3 Current and future climate SSA concentrations

Concentration is a function of emission and transport of the SSA, that is dependent on ventilation of an area over inner seas (wind speed), and on removal processes largely controlled by precipitation and relative humidity (via settling). Generally, the pattern of SSA concentration follows the emission areas with stronger winds and frequent storms. Concentrations are, therefore, higher at the Atlantic Ocean and lower at the European inner-seas. All the models show lower concentrations for the Baltic Sea, reaching up to 10 times difference from the ocean (Fig.5, left panel). The Mediterranean Sea is the inner sea with the highest concentrations. For the Baltic Sea, DEHM and MATCH show the highest and the lowest concentrations, respectively, with a difference of a factor of ~1.3 between each other. For the Black Sea, DEHM and EMEP show the highest concentrations and a similar spatial distribution pattern, and SILAM the lowest; nonetheless the difference is not so substantial. For the Mediterranean Sea, EMEP shows the lowest concentrations, MATCH being the highest: with 30% difference. All models show pronounced maximums at the Balearic Sea and the Levantine Sea. Transport over land is quite similar among the models, especially for the regional CTMs. The biggest difference lies over the western-central Europe with MATCH showing lower concentration over land. Transport of SSA is visible hundreds of km's inland; near the coastline it can contribute up to 6 $\mu g/m^3$ to PM_{10}.

The models predict relatively similar pattern for the SSA spatial distribution for the past period but they seem to have different responses to the future climate, with MATCH and SILAM clearly being the most sensitive and EMEP the least. Figure 5 (right panel) shows the difference between the past and future periods for the different models. DEHM and EMEP foresee almost no change or a decrease of SSA concentrations over the open sea, whereas MATCH and SILAM predict an increase. These results were expected due to the predicted emissions (Sect. 3.2). All models agree in an increase in SSA surface concentration over the north of Iceland, the Black Sea, and over land in southern latitudes. The models agree somehow on an increase of the Mediterranean and Black Seas SSA concentration but it is MATCH and SILAM that show the highest positive change in

concentrations. The impact over land is slightly positive for all the models in the Southern part of the domain, while at more Northern latitudes DEHM and EMEP from one side, and MATCH and SILAM models from another, disagree on the trend signal: a reduction of the SSA load over land is predicted by the first two models and an increase by the latter pair.

Overall, EMEP is the least sensitive and MATCH the most sensitive model to a changing climate. SILAM is the most sensitive over the Norwegian Sea. The difference between the past and future period concentrations is more substantial than that of emissions: the factors seemingly having exacerbated this difference are the decrease of ventilation over the west-Mediterranean, changes in mixing patterns, etc.

Trend analysis (supplementary material: Fig. S9 for the Baltic, Fig. S10 for the Black, Fig. S11 for the Mediterranean, and Fig. S12 for the North Seas) suggest that trends are only significant ($p < 0.001$) for MATCH and SILAM for both Mediterranean and Black seas, all with a positive signal.

Seasonally, the concentrations follow the same pattern as the emissions: higher in winter time. When analysing the changes between winter and summer, the models can again be grouped into DEHM-EMEP and MATCH-SILAM. In winter (Fig.6, left panel), the first pair presents a larger amount of SSA mass generally over sea and land surfaces. Conversely, MATCH and SILAM predict a decrease of SSA surface concentration around the British Isles, Mediterranean and Black Seas, though the coast lines have sharper peaks of SSA mass during winter. The difference between the future and past periods (Fig. 6, right panel) is relatively similar for all the models over the open sea: predictions show an increase of concentration around the British Isles and a decrease over the Norwegian Sea, in the future. MATCH and SILAM show sharper increase or decrease along the Mediterranean Sea. The changes predicted can be 3 times higher than the changes predicted for the emissions (Figure 4, right panel). The changes can also have different signal, e.g. the Eastern-basin of the Mediterranean where it is predicted an increase of emissions but a decrease of concentrations, implicating that the ventilation over this area was quite effective.

3.4 Current and future climate SSA deposition

The deposition (wet+dry) patterns for SSA are depicted in Fig. 7 (left panel). Typically the deposition is higher over the source areas and close to the coastal areas. Over land, SILAM shows less deposition and DEHM and EMEP predict the highest levels. There are different patterns over the Atlantic, mostly attributable to the boundary conditions treatment by each model. DEHM predicts quite high values over all the seas. Over the Black Sea, the deposition is more accentuated

in the predictions by EMEP and less by SILAM. MATCH also shows higher values for deposition over the Mediterranean, and SILAM the lowest. Deposition is not substantial over the Baltic Sea, with exception of DEHM, owing to low SSA mass released from its surface.

The impact of future climate conditions (Fig. 7, right panel) on deposition, in absolute levels, is small and mostly noticeable over the Atlantic Ocean. For all models, the most significant positive change in the deposition is seen around Iceland. This is expected according to the changes seen in precipitation between future and past periods (Fig. 1, third panel on the right). All regional CTMs show a strong signal on the west side of the domain, an artefact due to the boundary conditions. In relative terms, Scandinavia, east of UK, central-western Europe and the Mediterranean are the most affected with 5-20% more deposition predicted by MATCH and SILAM.

Trend analysis (supplementary material: Fig. S13 for the Baltic, Fig. S14 for the Black, Fig. S15 for the Mediterranean, and Fig. S16 for the North Seas) suggests that none of models show a significant trend.

Seasonally, SSA deposition is higher in winter than in summer, due to the higher emissions and frequent precipitation in winter months. This difference is mainly accentuated over the source areas: MATCH and SILAM have the lowest difference over the Baltic and Black Seas, due to the lower production; DEHM shows the highest at Mediterranean Sea. The difference of deposition between winter and summer will also change in the future period (Fig. 8, right panel) with all models showing a slight increase of the deposition in summer over the Mediterranean and along the coast of Norway. An increase of deposition in winter was suggested around Iceland and British Isles, North Sea and coastal areas of Mediterranean Sea.

4 Impact of meteorology and seawater properties on the emission and fate of SSA

The multi-model comparison presented in Sect. 3 shows that there are significant differences between the models in terms of emission and fate of the SSA. The latter is particularly true for the inner seas. The differences between the models lead to a more uncertain answer about the impact of the future climate on the production and transport of SSA and its possible feedback to climate. The SSA emission in the models is driven by three parameters: wind speed, water temperature, and water salinity. All models use the same $U_{10}^{3.41}$ dependence on wind speed; hence the differences in emission have to be attributed to parameterization of temperature and salinity dependencies. Formally, all models used the Monahan et al. (1986) and Mårtensson et al. (2003) parameterizations

or, at least, the available data for deriving the emission flux parametrizations (SILAM). Specifics of the implementation, however, appeared to cause a significant impact on the emission flux. To understand the latter, box-model calculations of the SSA mass flux as a function of temperature were made for seawater salinity 10 and 35 ‰, representing Baltic Sea and Atlantic Ocean, respectively, and with wind-speed fixed at 15 m/s (Fig. 9, left-hand panel).

In general, all the models show an increase of mass flux of SSA with temperature and salinity, except EMEP that does not apply any correction for salinity. Both DEHM and EMEP mass flux show little difference between low and high temperatures; SILAM and MATCH show a substantial dependency of the mass flux on temperature throughout the size ranges. This difference is explained by the way dependency on seawater temperature is implemented: only for the fine mode in DEHM and EMEP, based on the Mårtensson et al. (2003) source function, and for both fine and coarse modes in SILAM and MATCH. In MATCH, the implementation of seawater temperature correction is done by combining the temperature correction included in the Mårtensson et al. (2003) for size-range below Dp = 0.4 µm and the use of the temperature corrections from Sofiev et al. (2011) for the coarser sizes. In SILAM the source function is scaled with Sofiev et al. (2011) size-dependent temperature correction function. This explains why the results in Sect. 3 could be paired between the models. EMEP is the model that shows the highest amount of SSA produced, with the exception for seawater temperature higher than 15 ºC and high salinity, with MATCH and SILAM predicting the highest amount of SSA. For the lowest salinity, SILAM is the model that produces less SSA, with DEHM being surpassed by MATCH around 17 ºC. For the highest salinity, both MATCH and SILAM start to predict higher SSA flux than DEHM around 9 ºC. This is due to the temperature correction factor described in Sofiev et al. (2011) that assumes that for low seawater temperature, the production of coarse SSA, where the mass is significant, is very low. This analysis clarifies why MATCH and SILAM tend to have higher emissions than DEHM where waters are warmer and lower when colder (e.g. Baltic Sea), and why MATCH shows the highest values for the SSA mass flux. Also explains the smaller difference between winter and summer predicted by DEHM, since the changes in SSA mass flux depending on seawater temperature is very low.

Figure 9 (right panel) shows how the different models distribute the mass between the fine and coarse modes, for the same wind and salinity conditions described above. Both DEHM and EMEP assume that the contribution of the coarser mode is reduced with temperature, since more SSA is produced with higher temperatures, for size ranges below 2.5 µm. EMEP has the highest contribution for the coarse mode, independent of the temperature. For MATCH and SILAM, the

contribution to the coarser mode increases with temperature, though MATCH has a lower coarse mode contribution than SILAM. The only agreement between the DEHM, MATCH and SILAM is that for higher salinities, the coarse mode contribution is higher. The ratio between fine and coarse mode is very relevant for the deposition processes, and it could explain why deposition is higher for DEHM and EMEP (Fig. 7), though in this case, it is hard to evaluate the real impact due to different deposition schemes implemented in the models.

It is pertinent to discuss the difference between DEHM, EMEP and MATCH, since these models apply the same parameterization for SSA number flux, though having different salinity fields and salinity correction function. Mårtensson et al. (2003) defines very strict size ranges for the computation of the 6^{th} order polynomial for particles between 0.02 to 2.8 µm in dry diameter. In case the models define size ranges outside of the tabulated in that study, it can result in very different results. The linkage between the two parameterizations can also result in different outcomes: DEHM links the two parameterizations at dry diameter of 1.25 µm, EMEP at 1.5 µm and MATCH at 0.4 µm. In the case of MATCH, an extrapolation of the Monahan et al. (1996) function is needed, in order to bring it to Mårtensson et al. (2003) range.

5 SSA and climate change: production, fate and radiative impact

The regional-scale impact of SSA production and fate caused by a changing climate has been shown in Sect. 3. We show that the change in SSA emission between the past and future periods is not so large, arguably due to the small change in wind speed between the two time periods. Climates studies such as Gregow et al. (2011) projected higher wind speed changes in periods closer to the year 2100, in Scandinavia. Nevertheless, the available climate estimations of wind can differ substantially given the little understanding of how wind speed may change over the ocean in a warmer climate (IPCC, 2013). Studies such as Salisbury et al. (2013) suggest that other variables, in addition to wind forcing, influence the whitecap fraction, such as the seawater temperature or the sea state. New parameterization for whitecap fraction, based on satellite observations, claims that the whitecap-area based parameterization used by all the models in this study is misrepresenting the absolute values. Albert et al. (2015) suggests that for higher latitudes the values are overestimated, and underestimated for lower latitudes. If following that parameterization, the emission over the Mediterranean is underestimated. This could mean that the changes in seawater temperature would impact the SSA emission flux more substantially than suggested by this study.

555 The aerosol direct radiative effect (DRE) is defined as the difference between net radiative fluxes at
556 TOA in the presence and absence of SSA. The radiative forcing depends on the AOD of the aerosol
557 species in the atmosphere, the surface albedo and the vertical position of clouds. In this study, all-
558 sky conditions were considered, i.e. clouds are included. Over the seawater surfaces, SSA directly
559 scatters solar radiation back to space, resulting in a cooling effect on the climate by decreasing the
560 amount of radiation absorbed by the water surface. Over land, there can be both cooling over the
561 low-reflectance surfaces, and warming over high-albedo surfaces (e.g., Haywood and Boucher,
562 2000). Adding only a low absorbing aerosol, such as SSA, and assuming the same atmospheric and
563 cloud conditions for all the runs (with and without SSA), the upward scattering by SSA will be the
564 only radiation impact in this study.

565 Figure 10 shows the DRE due to SSA in the past (left panel) and the change in DRE due to the
566 changing climate (right panel). These calculations are based on the AOD predicted by SILAM for
567 the past and future. As expected, both past computations predict the highest cooling effect due to
568 SSA over the areas where concentrations (Fig. 5, left-lower panel) are the highest and where the
569 surface albedo is the lowest (seawater surfaces). The strongest effect is seen over the Mediterranean
570 Sea due to the lowest cloud cover and the largest number of hours of sunlight per year. Studies such
571 as Ma et al. (2008) and Lundgren et al. (2013), state that the impact of clouds can be substantial,
572 reducing the direct radiative impact of SSA. Less cooling effect is predicted where the albedo is
573 higher and SSA amount is the lowest. Conversely, cooling is predicted where the albedo is high due
574 to snow, e.g. over the mountain tops in Norway and Italy. The current study estimates the upward
575 scattering by SSA, at TOA, to be up to 0.5 W m^{-2} over seawater surfaces. This value is within the
576 estimates on upward scattering of radiation by SSA: ranging between 0.08 and 6 W m^{-2}, at
577 wavelengths in the range of 0.3-4 μm (Lewis and Schwartz, 2004). Figure 10, right panel, depicts
578 the change in the DRE due to SSA between future and past. The results suggest negative change in
579 DRE in the North and East of Europe and a positive change in the South-West of Europe. North of
580 Iceland, Norwegian and North Seas are the areas where the cooling is more accentuated. The
581 Mediterranean area seems to be again the most sensitive area in our study: an overall positive
582 change is predicted for this area, both over sea and land, meaning a reduction of radiative forcing in
583 the future due to SSA. A clear exception is predicted over the east of the eastern basin. The DRE
584 pattern for the whole year is highly influenced by the summer period due to largest number of
585 daylight hours. This can be seen in Fig. 11, right panel, which shows the change between future and
586 past but considering only the summer months (JJA). This study predicts a substantial seasonal
587 variation for the DRE in the sea surface waters. This is expected due to the variation shown in Sect.

588 3.2 and 3.3. The upward scattering in the summer time can be up to 1.7 times higher than in winter,
589 due to lower cloudiness and lengthier daylight.

590 Figure 11 shows the change in winter (left panel) and summer (right) between the future and the
591 past. The strongest impact in winter is seen over the Mediterranean area: negative over the sea
592 surface and positive over land. In summer, the highest impact is over the seawater surfaces,
593 predicting a cooling effect in the future, with exception over the western basin of the Mediterranean
594 and the western side of the British Isles and France.

595 The results presented in this study for the present period are in accordance with the regional
596 simulations for a summer month presented by Lundgren et al (2013) and the global simulations
597 presented by, e.g. Grini et al. (2002) and Ma et al. (2008). The results are shown in Table 5.

598 The radiative forcing estimation is sensitive to the quality of the input and the quantification of the
599 related uncertainty is cumbersome. The direct radiative forcing calculations will depend upon the
600 local atmospheric column burden of SSA in the atmosphere, the underlying surface reflectance, the
601 relative vertical position of the aerosol and the cloud, and the insolation. Evaluation of SILAM's
602 estimations for SSA shows a good agreement against in-situ and remote sensing observations, but
603 an overestimation can be expected due to the sensitivity of the SSA flux parameterization to
604 temperature (Witek et al, 2016). The surface albedo and cloud properties heavily rely on remote
605 sensing observations that have several constrains. The uncertainties of this data have been reported
606 in the literature and are referred to in Table 2. The averaging of hourly data to daily prior to
607 submitting them to radiative computations also introduce some limited uncertainty but it was
608 necessary due to the high computational demands of such computations. The direct radiative forcing
609 calculations also rely on the optical properties of the aerosol: the extinction coefficient, which
610 determines the degree of interaction of radiation and the aerosol particles; the single scattering
611 albedo, which determines the degree of absorption; and the scattering phase function, which
612 determines the angular distribution of scattered radiation (e.g. Kiehl and Briegleb, 1993). Sensitivity
613 studies considering the parameters describing the SSA were made. For example, setting the SSA's
614 single scattering albedo as low as 0.95 (Russel et al, 2002), leads to a wide areas over land where
615 warming is substantial: essentially, over all surfaces with albedos exceeding 0.5 and low (<0.03)
616 aerosol load (not shown). We have chosen to show results for a more realistic SSA single scattering
617 albedo of 0.99 (Lundgren et al., 2013). On the other hand, varying other aerosol properties such as
618 asymmetry factor or angstrom coefficient has no substantial influence on the final result.

Besides contributing to the DRE, SSA can have a major impact on modifying the cloud optical and physical properties. It has been commonly believed that increasing aerosol concentrations is likely to inhibit rainfall via aerosol indirect effect, which tends to reduce rainfall efficiency of the low-level warm clouds (e.g. Ramanathan et al. 2001). Being a naturally large aerosol, especially if generated by the tearing of droplets from the top of breaking waves, the SSA may be directly activated to CCN and readily initiate the warm-rain processes (Chen et al, 2007). These so-called giant nuclei may override the precipitation suppression effect of the large number of small pollution nuclei (e.g. Rosenfeld et al., 2002) and may contribute to warming by decreasing the cloud amount due to increasing precipitation (Lohmann and Feichter, 2005). However, this topic is left out of the current paper since the models needed for simulation of aerosol-cloud interactions are completely different from the tools used in our study.

6 Conclusion

This study has compared predictions of SSA emissions, surface concentration and deposition from four CTMs for both current condition and future scenarios, focusing on the European Seas: Baltic, North, Mediterranean, and Black Seas. The three European-scale CTMs (EMEP, MATCH and SILAM) were driven by the regional climate model (RCA3) meteorology and by the hemispheric model (DEHM) boundary conditions. The hemispheric model was driven by the ECHAM5 meteorology. The impact of climate change on SSA production and fate, due to changes in wind speed and seawater temperature, was analysed. Additionally, consideration about the impact of seawater salinity on emissions was given.

The impact of climate change on SSA production and fate has different response from the models, with the similar results between DEHM and EMEP, and between MATCH and SILAM. DEHM-EMEP show almost no difference between future and past periods, and MATCH-SILAM shows a general increase of the emissions and surface concentrations with levels reaching 30% in change. The emissions increase is substantial in the Black Sea, Gulf of Bothnia (Baltic) and Levantine Sea (Mediterranean), correlating well with the wind-forcing ($\approx U_{10}^{3.41}$) computed with the changes predicted between the same periods. Nevertheless, the major driver of the changes of the sea-salt fluxes from the sea surface will be the changing seawater temperature, since near-surface wind speed is projected to stay nearly the same in the climate scenario used; in absolute levels the wind will change less than a meter per second, on average, between the two periods. The concentrations are predominantly increasing in Black and Mediterranean Sea. The impact of climate change on

SSA deposition is not really relevant; though an increase is projected around Iceland by all the models. Boundary conditions impact on the predictions is substantial.

The discrepancies between the models raised additional questions about the implementation of the SSA production formulations, since three of the models are based on the same parameterizations. This study shows that temperature and salinity correction functions play an important role for the final scaling of the SSA flux and how aerosol size range prescription may play a substantial role on the SSA flux calculation.

Simple calculations with the libRadTran allowed understanding the impact of SSA on the direct radiative forcing. According to this study the upward scattering by SSA, at TOA, can to be up to 0.5 W m^{-2} and an average value of 0.12 W m^{-2} over the seawater surfaces in the present period, predicting an overall cooling in the future. The most affected areas by cooling will be North of Iceland, Norwegian and North Seas, and the eastern basin of the Mediterranean; warming is predicted mainly in Mediterranean Sea, including over land.

Acknowledgements

This study was supported by the Nordic Council of Ministers through EnsCLIM and CarboNord projects, and by the Academy of Finland though the APTA project. The authors also thank Antti Arola for his guidance in the radiative forcing calculations and interpretation of the results.

References

Albert, M. F. M. A., Anguelova, M. D., Manders, A. M. M., Schaap, M., and de Leeuw, G.: Parameterization of oceanic whitecap fraction based on satellite observations, Atmos. Chem. Phys. Discuss., 15, 21219-21269, doi:10.5194/acpd-15-21219-2015, 2015.

Andersson, C., Bergström, R., Bennet, C., Robertson, L., Thomas, M., Korhonen, H., Lehtinen, K. E. J., and Kokkola, H.: MATCH-SALSA – Multi-scale Atmospheric Transport and CHemistry model coupled to the SALSA aerosol microphysics model – Part 1: Model description and evaluation, Geosci. Model Dev., 8, 171-189, doi:10.5194/gmd-8-171-2015, 2015.

Andreas, E. L.: A new sea spray generation function for wind speeds up to 32 m s−1, J. Phys. Oceanogr., 28, 2175–2184, doi:10.1175/1520-0485(1998)028<2175:ANSSGF>2.0.CO;2., 1998

680 Andreas, E. L., Edson, J. B., Monahan, E. C., Rouault, M. P., and Smith, S. D.: The spray
681 contribution to net evaporation from the sea: A review of recent progress, Boundary Layer
682 Meteorol., 72(1–2), 3–52, doi:10.1007/BF00712389, 1995.

683 Bates, T. S., Coffman, D. J., Covert, D. S., and Quinn, P. K.: Regional marine boundary layer
684 aerosol size distributions in the Indian, Atlantic, and Pacific Oceans: A comparison of INDOEX
685 measurements with ACE-1, ACE-2, and Aerosols99, J. Geophys. Res., 107(D18), 8026,
686 doi:10.1029/2001JD001174, 2002.

687 Bellouin, N., Rae, J., Jones, A., Johnson, C., Haywood, J., and Boucher, O.: Aerosol forcing in the
688 Climate Model Intercomparison Project (CMIP5) simulations by HadGEM2-ES and the role of
689 ammonium nitrate, J. Geophys. Res., 116, D20206, doi:10.1029/2011JD016074, 2011.

690 Boyer, T. P., Levitus S., Garcia, H. E., Locarnini, R. A., Stephens, C., Antonov, J. I.; Objective
691 analyses of annual, seasonal, and monthly temperature and salinity for the world ocean on a 0.25
692 degrees grid. Int. J. Climatol. 25 (7), 931-945, 2005.

693 Boyd, P. W.: Ranking geo-engineering schemes, Nat. Geosci., 1, 722–724, doi:10.1038/ngeo348,
694 2008.

695 Brandt J, Silver, J., Frohn, L. M., Geels, C., Gross, A., Hansen, A. B., Hansen, K. M., Hedegaard,
696 G. B., Skjøth, C. A., Villadsen, H., Zare, A., and Christensen, J. H.: An integrated model study
697 for Europe and North America using the Danish Eulerian Hemispheric Model with focus on
698 intercontinental transport of air pollution. Atmos.Environ. 53:156-176, 2012.

699 Chen, R., Chang, F-L., Li, Z., Ferraro, R., and Weng, F.: Impact of the Vertical Variation of Cloud
700 Droplet Size on the Estimation of Cloud Liquid Water Path and Rain Detection. J. Atmos. Sci.,
701 64, 3843–3853, doi: 10.1175/2007JAS2126.1, 2010

702 Covert, D. S., Gras, J. L, Wiedensohler, A., and Stratmann, F.: Comparison of directly measured
703 CCN with CCN modeled from the number-size distribution in the marine boundary layer during
704 ACE I at Cape Grim, Tasmania, J. Geophys. Res., 103, 16,597-16,608, 1998.

705 de Leeuw, G., Andreas, E. L, Anguelova, M. D., Fairall, C. W., Lewis, E. R., O'Dowd, C., Schulz,
706 M. and Schwartz, S. E.: Production flux of sea spray aerosol, Rev. Geophys., 49, RG2001,
707 doi:10.1029/2010RG000349, 2011.

708 Dana, M. T., and Hales, J. M.; Statistical aspects of the washout of polydisperse aerosols. Atmos.
709 Environ. 10, 45-50, 1976.

710 Emberson, L. D., Ashmore, M. R., Cambridge, H. M., Simpson, D., and Tuovinen, J. P.: Modelling
711 stomatal ozone flux across Europe, Environ. Pollut., 109, 403–413, 2000.

712 Foltescu, V. L., Pryor, S. C. and Bennet, C.: Sea salt generation, dispersionand removal on the
713 regional scale. Atmospheric Environment 39, 2123-2133, 2005.

714 Gregow, H., Ruosteenoja, K., Pimenoff, N., and Jylhä, K.: Changes in the mean and extreme
715 geostrophic wind speeds in Northern Europe until 2100 based on nine global climate models. Int.
716 J. Climatol., 32, 1834–1846, 2011.

717 Grini, A., Myhre, G., Sundet, J. K., and Isaksen, I. S. A.: Modeling the annual cycle of sea salt in
718 the global 3D model OsloCTM2: Concentrations, fluxes, and radiative impact, J. Climate, 15,
719 1717–1730, 2002.

720 Gong, S. L.: A parameterization of sea-salt aerosol source function for sub- and super-micron
721 particles, Global Biogeochem. Cycles, 17(4), 1097, doi:10.1029/2003GB002079, 2003.

722 Gong, S. L., Barrie, L. A., Prospero, J. M., Savoie, D. L., Ayers, G. P., Blanchet, J.-P., and Spacek,
723 L.: Modelling sea-salt aerosols in the atmosphere: 2. Atmospheric concentrations and fluxes, J.
724 Geophys. Res., 102(D3), 3819–3830, doi:10.1029/96JD03401, 1997.

725 Haywood, J., and Boucher, O.: Estimates of the direct and indirect radiative forcing due to
726 tropospheric aerosols: A review, Rev. Geophys., 38(4), 513–543, doi:10.1029/1999RG000078,
727 2000.

728 Haywood, J., Ramaswamy, V., and Soden, B.: Tropospheric aerosol climate forcing in clear-sky
729 satellite observations over the oceans, Science, 283, 1299– 1303, 1999.

730 Hjellbrekke, A.-G. & Fjæra, A. M.: Data Report: Acidifying and eutrophying compounds and
731 particulate matter. EMEP/CCC-Report 1/2011, 2009.

732 Horn, H., Bonka, H., and Maqua, M.: Measured particle bound activity size-distribution, deposition
733 velocity, 700 and activity concentration in rainwater after the Chernobyl accident, J. of Aerosol
734 Science, 18, 681–684, 10.1016/0021-8502(87)90096-6, 1987.

735 Huebert, B. J., Bates, T., Russell, P. B., Shi, G., Kim, Y. J., Kawamura, K., Carmichael, G., and
736 Nakajima, T.: An overview of ACE-Asia: Strategies for quantifying the relationships between
737 Asian aerosols and their climatic impacts, J. Geophys. Res., 108(D23), 8633,
738 doi:10.1029/2003JD003550, 2003.

739 IPCC: Climate Change 2013: The Physical Science Basis. Contribution of Working Group I to the
740 Fifth Assessment Report of the Intergovernmental Panel on Climate Change [Stocker, T.F., D.
741 Qin, G.-K. Plattner, M. Tignor, S.K. Allen, J. Boschung, A. Nauels, Y. Xia, V. Bex and P.M.
742 Midgley (eds.)]. Cambridge University Press, Cambridge, United Kingdom and New York, NY,
743 USA, 1535 pp, doi:10.1017/CBO9781107415324, 2013

744 Jylhä, K.: Empirical scavenging coefficients of radioactive substances released from Chernobyl,
745 Atmos. Environ. A., 25, 263–270, 10.1016/0960-1686(91)90297-K, 1991.

746 Kaskaoutis, D. G., Kambezidis, H. D., Hatzianastassiou, N., Kosmopoulos, P. G., and
747 Badarinath, K. V. S.: Aerosol climatology: dependence of the Angstrom exponent on wavelength
748 over four AERONET sites, Atmos. Chem. Phys. Discuss., 7, 7347-7397, doi:10.5194/acpd-7-
749 7347-2007, 2007.

750 Kiehl, J. T. and Briegleb, B.P.: The relative roles of sulfate aerosols and greenhouse gases in
751 climate forcing, Science, 260, 311–314, 1993.

752 Kjellström, E., Nikulin, G., Hansson, U., Strandberg, G., and Ullerstig, A.: 21st century changes in
753 the European climate: uncertainties derived from an ensemble of regional climate model
754 simulations, Tellus Series A-Dynamic Meteorology and Oceanography, 63, 24–40,
755 10.1111/j.1600-0870.2010.00475.x, 2011.

756 Kusmierczyk-Michulec J. and van Eijk, A.M.J.: Atmospheric Optics: Models, Measurements, and
757 Target-in-the-Loop Propagation III, 74630G; Stephen M. Hammel; Alexander M. J. van Eijk;
758 Mikhail A. Vorontsov, Editor(s) doi: 10.1117/12.828394, 2009.

759 Korhonen, H., K. Carslaw, S., and Romakkaniemi, S.: Enhancement of marine cloud albedo via
760 controlled sea spray injections: A global model study of the influence of emission rates,
761 microphysics and transport, Atmos. Chem. Phys., 10, 4133–4143, doi:10.5194/acp-10-4133-
762 2010, 2010.

763 Kouznetsov, R. and Sofiev, M.: A methodology for evaluation of vertical dispersion and dry
764 deposition of atmospheric aerosols, J. Geophys. Res., 117, 10.1029/2011JD016366, 2012.

765 Langner, J., Engardt, M., and Andersson, C.: European summer surface ozone 1990–2100, Atmos.
766 Chem. Phys., 12, 10097-10105, doi:10.5194/acp-12-10097-2012, 2012.

767 Latham, J., and Smith, M. H.: Effect on global warming of wind dependent aerosol generation at the
768 ocean surface, Nature, 347, 372–373, doi:10.1038/347372a0, 1990.

769 Lenton, T. M., and Vaughan, N. E.: The radiative forcing potential of different climate
770 geoengineering options, Atmos. Chem. Phys., 9, 5539–5561, doi:10.5194/acp-9-5539-2009,
771 2009.

772 Lewis, E. R., and Schwartz, S. E.: Comment on "Size distribution of sea-salt emissions as a
773 function of relative humidity," Atmos. Environ., 40, 588–590,
774 doi:10.1016/j.atmosenv.2005.08.043, 2006.

775 Liao, H., Chen, W. T., and Seinfeld, J. H.: Role of climate change in global predictions of future
776 tropospheric ozone and aerosols. J. Geophys. Res., 111, D12304, 2006.

777 Lohmann, U., and Feichter, J.: Global indirect aerosol effects: A review, Atmos. Chem. Phys., 5,
778 715– 737, 2005.

779 Lundgren, K., Vogel, B.,Vogel, H., and Kottmeier, C.: Direct radiative effects of sea salt for the
780 Mediterranean region under conditions of low to moderate wind speeds, J. Geophys. Res.
781 Atmos., 118, 1906–1923, doi:10.1029/2012JD018629, 2013.

782 Ma, X., von Salzen, K., and Li, J.: Modelling sea salt aerosol and its direct and indirect effects on
783 climate, Atmos. Chem. Phys., 8, 1311-1327, doi:10.5194/acp-8-1311-2008, 2008.

784 Mahowald, N. M., Lamarque, J.-F., Tie, X. X., and Wolff, E.: Sea-salt aerosol response to climate
785 change: Last Glacial Maximum, preindustrial, and doubled carbon dioxide climates, J. Geophys.
786 Res., 111, D05303, doi:10.1029/2005JD006459, 2006.

787 Manders, A. M. M., Schap, M., Querol, X., Albert, M. F., Vercauteren, J., Kuhlbusch, T. A. J., and
788 Hoogerbrugge, R.: Sea salt concentrations across the European continent, Atmos. Environ., 44,
789 2434–2442, doi:10.1016/j.atmosenv.2010.03.028, 2010.

790 Mayer, B. and Kylling, A.: Technical note: The libRadtran software package for radiative transfer
791 calculations - description and examples of use, Atmos. Chem. Phys., 5, 1855-1877,
792 doi:10.5194/acp-5-1855-2005, 2005.

793 Mie, G.: Beiträge zur Optik trüber Medien, speziell kolloidaler Metallösungen [Contribution to the
794 optics of turbid media, particularly of colloquial metal solutions Royal Aircraft Establishment],
795 Ann. Phys.25(3), 377–445, 1908.

796 Monahan, E. C., Spiel, D. E., and Davidson, K. L.: A model of marine aerosol generation via
797 whitecaps and wave disruption, in Oceanic Whitecaps, edited by E. C. Monahan and G.
798 MacNiochaill, 167–193, D. Reidel, Norwell, Mass, 1986.

Mårtensson, E. M., Nilsson, E. D., de Leeuw, G., Cohen, L. H., and Hansson, H.-C.: Laboratory simulations and parameterization of the primary marine aerosol production, J. Geophys. Res., 108(D9), 4297, doi:10.1029/2002JD002263, 2003

Nakićenović, N.: Global greenhouse gas emissions scenarios: Integrated modeling approaches, Tech. Forecasting & Social Change, 63, 105–109, 2000.

Nilsson, E. D., Mårtensson, E. M., van Ekeren, J. S., de Leeuw, G., Moerman, M. M., and O'Dowd, C. D.: Primary marine aerosol emissions: Size resolved eddy covariance measurements with estimates of the sea salt and organic carbon fractions, Atmos. Chem. Phys. Discuss., 7, 13,345–13,400, doi:10.5194/acpd-7-13345-2007, 2007.

NOAA: World Ocean Atlas 2013. http://www.nodc.noaa.gov/OC5/woa13/, 2013

O'Dowd, C., and de Leeuw, G.: Marine aerosol production: A review of the current knowledge, Philos. Trans. R. Soc. A, 365, 1753–1774, doi:10.1098/rsta.2007.2043, 2007.

O'Dowd, C. D., and Smith, M. H.: Physico-chemical properties of aerosol over the North East Atlantic: Evidence for wind speed related sub-micron sea-salt aerosol production, J. Geophys. Res., 98, 1137–l149, doi:10.1029/92JD02302, 1993.

O'Dowd, C., Lowe, J., Smith, M., and Kaye, A.: The relative importance of non-seasalt sulphate and sea-salt aerosol to the marine cloud condensation nuclei population: An improved multi-component aerosolcloud droplet parameterization, Q. J. R. Meteorol. Soc., 125, 1295–1313, 1999.

O'Dowd, C. D., Smith, M. H. Consterdine, I. E., and Lowe, J. A.: Marine aerosol, sea salt, and the marine sulphur cycle: A short review, Atmos. Environ., 31, 73–80, doi:10.1016/S1352-2310(96)00106-9, 1997

Ovadnevaite, J., Manders, A., de Leeuw, G., Ceburnis, D., Monahan, C., Partanen, A.-I., Korhonen, H., and O'Dowd, C. D.: A sea spray aerosol flux parameterization encapsulating wave state, Atmos. Chem. Phys., 14, 1837-1852, doi:10.5194/acp-14-1837-2014, 2014.

Pierce, J. R., and Adams, P. J.: Global evaluation of CCN formation by direct emission of sea salt and growth of ultrafine sea salt, J. Geophys. Res., 111, D06203, doi:10.1029/2005JD006186, 2006.

827 Pincus, R., Platnick, S., Ackerman, S. A., Hemler, R. S., and Hofmann, R. J. P.: Reconciling
828 simulated and observed views of clouds: MODIS, ISCCP, and the limits of instrument
829 simulators, Journal of Climate, 2011.

830 Pryor, S. C., and Barthelmie, R. J.: Particle dry deposition to water surfaces: processes and
831 consequences. Marine Pollution Bulletin 41, 220-231, 2000.

832 Prank, M.: Evaluation of atmospheric composition simulations via comparison with remote-sensing
833 and in-situ observations, Master's thesis, 74 pp., Dep. of Sci. and Technol., Univ. of Tartu,
834 Tartu, Estonia, 2008.

835 Quinn, P. K., Coffman, D. J., Kapustin, V. N., Bates, T. S., Covert, D. S.: Aerosol optical properties
836 in the marine boundary layer during the First Aerosol Characterization Experiment (ACE 1) and
837 the underlying chemical and physical aerosol properties, J. Geophys. Res., 103, D13, 547-
838 16,563, 1998

839 Ramanathan, V., Crutzen, P. J., Kiehl, J. T., andRosenfeld, D.: Aerosols, climate, and the
840 hydrological cycle. *Science*, 294, 2119–2124, 2001.

841 Roeckner, E., Brokopf, R., Esch, M., Giorgetta, M., Hagemann, S., Kornblueh, L., Manzini, E.,
842 Schlese, U., and Schulzweida, U.: Sensitivity of simulated climate to horizontal and vertical
843 resolution in the ECHAM5 atmosphere model, J. Clim., 19, 3771–3791, 10.1175/JCLI3824.1,
844 2006.

845 Rodell, M., Houser, P.R., Jambor, U., Gottschalck, J., Mitchell, K., Meng, C.-J., Arsenault, K.
846 Cosgrove, B., Radakovich, J., Bosilovich, M., Entin, J.K., Walker, J.P., Lohmann, D., and Toll,
847 D.: The Global Land Data Assimilation System, Bull. Amer. Meteor. Soc., 85(3), 381-394, 2004

848 Russel, P.B., and Heintzenberg, J.: An overview of the ACE-2 clear sky column closure experiment
849 (CLEARCOLUMN). Tellus B, [S.l.], 52(2), ISSN 1600-0889,
850 doi:http://dx.doi.org/10.3402/tellusb.v52i2.16173, 2011.

851 Russell, P. B., Redemann, J., Schmid, B., Bergstrom., R. W., Livingston, J. M., McIntosh, D. M.,
852 Ramirez, S. A., Hartley, S., Hobbs, P. V., Quinn, P. K., Carrico, C. M., Rood, M. J., Öström, E.,
853 Noone, K. J., von Hoyningen-Huene, W., and Remer, L.: Comparison of Aerosol Single
854 Scattering Albedos Derived by Diverse Techniques in Two North Atlantic Experiments. J.
855 Atmos. Sci., 59, 609–619, doi: http://dx.doi.org/10.1175/1520-
856 0469(2002)059<0609:COASSA>2.0.CO;2, 2002

857 Salisbury, D. J., Anguelova, M. D., and Brooks, I. M.: On the variability of whitecap fraction using
858 satellite-based observations, J. Geophys. Res.-Oceans, 118, 6201–6222, 2013.

859 Samuelsson, Jones, P., Willén, C. G., Ullerstig, U., Gollvik, A., Hansson, S., Jansson, U.,
860 Kjellström, C., Nikulin, E., and Wyser, K.: The Rossby Centre Regional Climate model RCA3:
861 Model description and performance, Tellus A, 63, 4–23, doi:10.111/j.1600-0870.2010.00478.x,
862 2011.

863 Seinfield, J. H., and Pandis, S. N.: Atmospheric Chemistry and Physics: From Air Pollution to
864 Climate Change, 2nd ed., 1232, John Wiley, Hoboken, N. J., 2006.

865 Simpson, D., Andersson, C., Christensen, J.H., Engardt, M., Geels, C., Nyiri, A., Posch, M., Soares,
866 J., Sofiev, M., Wind, P., and Langner, J.: Impacts of climate and emission changes on nitrogen
867 deposition in Europe: a multi-model study, Atmos. Chem. Phys., 14, 6995-7017,
868 doi:10.5194/acp-14-6995-2014, 2014.

869 Simpson, D., Fagerli, H., Jonson, J. E., Tsyro, S., Wind, P., and Tuovinen, J.-P: Transboundary
870 Acidification, Eutrophication and Ground Level Ozone in Europe, PART I, Unified EMEP
871 Model Description, 1-104, 2003.

872 Smith, F. B., and Clark, M. J.: The transport and deposition of radioactive debris from the
873 Chernobyl nuclear power plant accident with special emphasis on consequences to the United
874 Kingdom, Meteorological Office Scientific Paper no. 42, HMSO London, 1989.

875 Sofiev, M., Siljamo, P., Valkama, I., Ilvonen, M., and Kukkonen, J.: A dispersion modelling system
876 SILAM and its evaluation against ETEX data, Atmos. Environ., 40, 674–685,
877 10.1016/j.atmosenv.2005.09.069, 2006.

878 Sofiev, M., Soares, J., Prank, M., de Leeuw, G., and Kukkonen, J.: A regional-to-global model of
879 emission and transport of sea salt particles in the atmosphere, J. Geophys. Res., 116, D21302,
880 doi:10.1029/2010JD014713, 2011.

881 Struthers, H., Ekman, A. M. L., Glantz, P., Iversen, T., Kirkevåg, A., Mårtensson, E. M., Seland,
882 Ø., and Nilsson, E. D.: The effect of sea ice loss on sea salt aerosol concentrations and the
883 radiative balance in the Arctic, Atmos. Chem. Phys., 11, 3459-3477, doi:10.5194/acp-11-3459-
884 2011, 2011.

885 Tsyro, S., Aas, W., Soares, J., Sofiev, M., Berge, H., and Spindler, G.: Modelling of sea salt
886 pollution over Europe: key uncertainties and comparison with observations Atmos. Chem. Phys.,
887 11, 10367-10388, doi:10.5194/acp-11-10367-2011, 2011.

888 Textor, C., Schulz, M., Guibert, S., Kinne, S., Balkanski, Y., Bauer, S., Berntsen, T., Berglen, T.,
889 Boucher, O., Chin, M., Dentener, F., Diehl, T., Easter, R., Feichter, H., Fillmore, D., Ghan, S.,
890 Ginoux, P., Gong, S., Grini, A., Hendricks, J., Horowitz, L., Huang, P., Isaksen, I., Iversen, I.,
891 Kloster, S., Koch, D., Kirkevåg, A., Kristjansson, J. E., Krol, M., Lauer, A., Lamarque, J. F.,
892 Liu, X., Montanaro, V., Myhre, G., Penner, J., Pitari, G., Reddy, S., Seland, Ø., Stier, P.,
893 Takemura, T., and Tie, X.: Analysis and quantification of the diversities of aerosol life cycles
894 within AeroCom, Atmos. Chem. Phys., 6, 1777-1813, doi:10.5194/acp-6-1777-2006, 2006.

895 Twomey S.: Atmospheric Aerosol, Elviser, Amesterdam, 1977.

896 Tørseth, K., Aas, W., Breivik, K., Fjæraa, A. M., Fiebig, M., Hjellbrekke, A. G., Lund Myhre, C.,
897 Solberg, S., and Yttri, K. E.: Introduction to the European Monitoring and Evaluation
898 Programme (EMEP) and observed atmospheric composition change during 1972–2009, Atmos.
899 Chem. Physics, 12, 5447–5481, 10.5194/acp-12-5447-2012, http://www.atmos-chem-
900 phys.net/12/5447/2012/, 2012.

901 Wang, M., Ghan, S., Ovchinnikov, M., Liu, X., Easter, R., Kassianov, E., Qian, Y., and Morrison,
902 H.: Aerosol indirect effects in a multi-scale aerosol-climate model PNNL-MMF, Atmos. Chem.
903 Phys., 11, 5431-5455, doi:10.5194/acp-11-5431-2011, 2011.

904 Witek, M. L., D. J. Diner, and M. J. Garay: Satellite assessment of sea spray aerosol productivity:
905 Southern Ocean case study, J. Geophys. Res. Atmos., 121, doi:10.1002/2015JD023726, 2016.

906 Witek, M. L., P. J. Flatau, J. Teixeira, and K. M. Markowicz: Numerical investigation of sea salt
907 aerosol size bin partitioning in global transport models: Implications for mass budget and optical
908 depth, Aerosol Sci. Technol., 45, 401–414, doi:10.1080/02786826.2010.541957, 2011.

909 Witek, M. L., Flatau, P. J., Quinn, P. K., and Westphal, D. L.: Global sea-salt modeling: Results
910 and validation against multicampaign shipboard measurements, J. Geophys. Res., 112, D08215,
911 doi:10.1029/2006JD007779, 2007a.

912 Witek, M. L., Flatau, P. J., Teixeira, K., and Westphal, D. L: Coupling an ocean wave model with a
913 global aerosol transport model: A sea salt aerosol parameterization perspective, Geophys. Res.
914 Lett., 34, L14806, doi:10.1029/2007GL030106, 2007b.

van Loon, M., Tarrasón, L., and Posch, M.: Modelling Base Cations in Europe, Technical Report MSC-W, Norwegian Meteorological Institute, ISSN 0804-2446, 2005

Zhang, L., Gong, S., Padro, J., and Barrie, L.: A size-segregated particle dry deposition scheme for an atmospheric aerosol module. Atmospheric Environment 35, 549-560., 2001.

Table 1 Model characteristics for SSA computations.

model	mode	Dp [µm]	source function	dependency	humidity	Lowest model layer thickness (m)
DEHM	fine	<1.3	MA02	T S	static (80%)	60
	coarse	[1.3-10]	MO86	S		
EMEP	fine	<2.5	MA02	T	static (80%)	90
	coarse	[2.5-10]	MO86	-		
MATCH	fine	[0.02–0.1] [0.1–1] [1–2.5]	MA02	T S	dynamic	60
	coarse	[2.5–10]	MO86	T (SO11**)** S		
SILAM	fine	[0.01–0.1] [0.1–1.5]	SO11	T S	dynamic	25
	coarse	[1.5–6]				
		[6–15]	SO11	T S		
		[15-30]				

T: temperature, **S**: salinity, **MO86**: Monahan et al. (1986); **MA03**: Mårtensson et al. (2003), **SO11**: Sofiev et al. (2011). In bold, the modes not used for the PM_{10} analysis.

927 Table 2 Assumption for the radiative transfer modelling libRadTran2.0 for present and future.

Clouds (icy and wet)	cloud cover	monthly averaged RCA3 fields (1990-2009); same for both periods
	AOD	monthly averaged MODIS data (2002-2014) (Pincus et al. 2011); same for both periods
	vertical profiles	wc.dat*; ic.dat*
Atmospheric properties	vertical profiles	subarctic winter, latitude over 60°: afglsw.dat* subarctic summer, latitude over 60°: afglss.dat* mid-latitude winter, latitude below 60°: afglmw.dat* mid-latitude summer, latitude below 60°: afglms.dat*
	altitude, pressure and temperature	monthly averaged RCA3 fields (1990-2009); same for both periods
Aerosol properties	vertical profile	aerosol_default*
	AOD	dynamic: SILAM AOD calculations
	asymmetry factor	0.8 (Ma et al. 2008)
	single scattering albedo	0.99 (Lundgren et al, 2013)
	angstrom coefficient	0.2 (Kaskaoutis et al, 2007; Kusmierczyk-Michulec & van Eijk, 2009)
solar zenith angle		dynamic: computed with libRadTran sza tool
surface albedo		monthly averaged NOAA data (1990-2012) (Rodell et al., 2004); same for both periods
RTE solver		DISORT
integrated shortwave calculation scheme		KATO2 (wavelength ~[0.2, 4] μm)

928 *****standard file in libRadTran

929

930 Table 3 Statistical evaluation of model results for surface SSA concentration ($\mu gNa^{+}\ m^{-3}$),
931 considering the whole year (annual), winter (December, January and February) and summer
932 periods (June, July and August), for 33 EMEP measuring sites, between 1990 and 2009.

	annual	**winter**	**summer**	**annual**	**winter**	**summer**
		mean				
Obs	0.72	0.94	0.55			
DEHM	1.08	1.39	0.74			
EMEP	0.64	0.75	0.49			
MATCH	0.45	0.42	0.42			
SILAM	0.86	0.78	0.94			
		correlation coefficient			StdRatio	
DEHM	0.85	0.87	0.81	1.72	1.57	1.79
EMEP	0.82	0.84	0.80	0.69	0.54	0.85
MATCH	0.75	0.82	0.77	0.48	0.33	0.66
SILAM	0.71	0.77	0.75	1.05	0.75	1.59
		RMSE			Bias	
DEHM	0.97	1.11	0.70	0.36	0.45	0.18
EMEP	0.53	0.75	0.36	-0.08	-0.18	-0.06
MATCH	0.69	1.03	0.41	-0.27	-0.52	-0.14
SILAM	0.71	0.76	0.74	0.14	-0.16	0.38

933
934

Table 4 Statistical evaluation of model results for SSA wet deposition, considering the accumulated deposition over the whole year (mgNa^+ m^{-2} y^{-1}), winter (December, January and February) and summer periods (June, July and August) (mgNa^+ m^{-2} $period^{-1}$), for 133 EMEP measurement sites, between 1990 and 2009. SILAM5m is the evaluation if considering the whole possible size range for SSA Dp = [0.01-30] μm.

	annual	**winter**	**summer**	**annual**	**winter**	**summer**
		mean				
obs	1.59E+06	6.88E+05	1.36E+05			
DEHM	1.41E+06	5.59E+05	1.40E+05			
EMEP	1.64E+06	6.44E+05	1.65E+05			
MATCH	6.08E+05	1.77E+05	9.64E+04			
SILAM	8.42E+05	2.81E+05	1.25E+05			
SILAM5m	1.70E+06	6.70E+05	1.83E+05			
		correlation coefficient			StdRatio	
DEHM	0.55	0.53	0.41	0.36	0.31	0.55
EMEP	0.38	0.32	0.33	0.47	0.44	0.53
MATCH	0.49	0.50	0.34	0.13	0.11	0.26
SILAM	0.49	0.45	0.38	0.22	0.19	0.41
SILAM5m	0.62	0.63	0.37	0.86	0.84	0.93
		RMSE			Bias	
DEHM	3477	5513	866	-114	-327	10
EMEP	3778	6006	912	34	-112	74
MATCH	3879	6122	892	-634	-1304	-102
SILAM	3737	5945	871	-483	-1038	-29
SILAM5m	3335	5070	1032	73	-44	122

942 Table 5 Predicted direct radiative effect (W m^{-2}) by SSA for the past period

	annual	**winter**	**summer**
sea	-0.25±0.22	-0.077±0.053	-0.21±0.012
land	-0.20±0.18	-0.073±0.0019	-0.083±0.0030

943

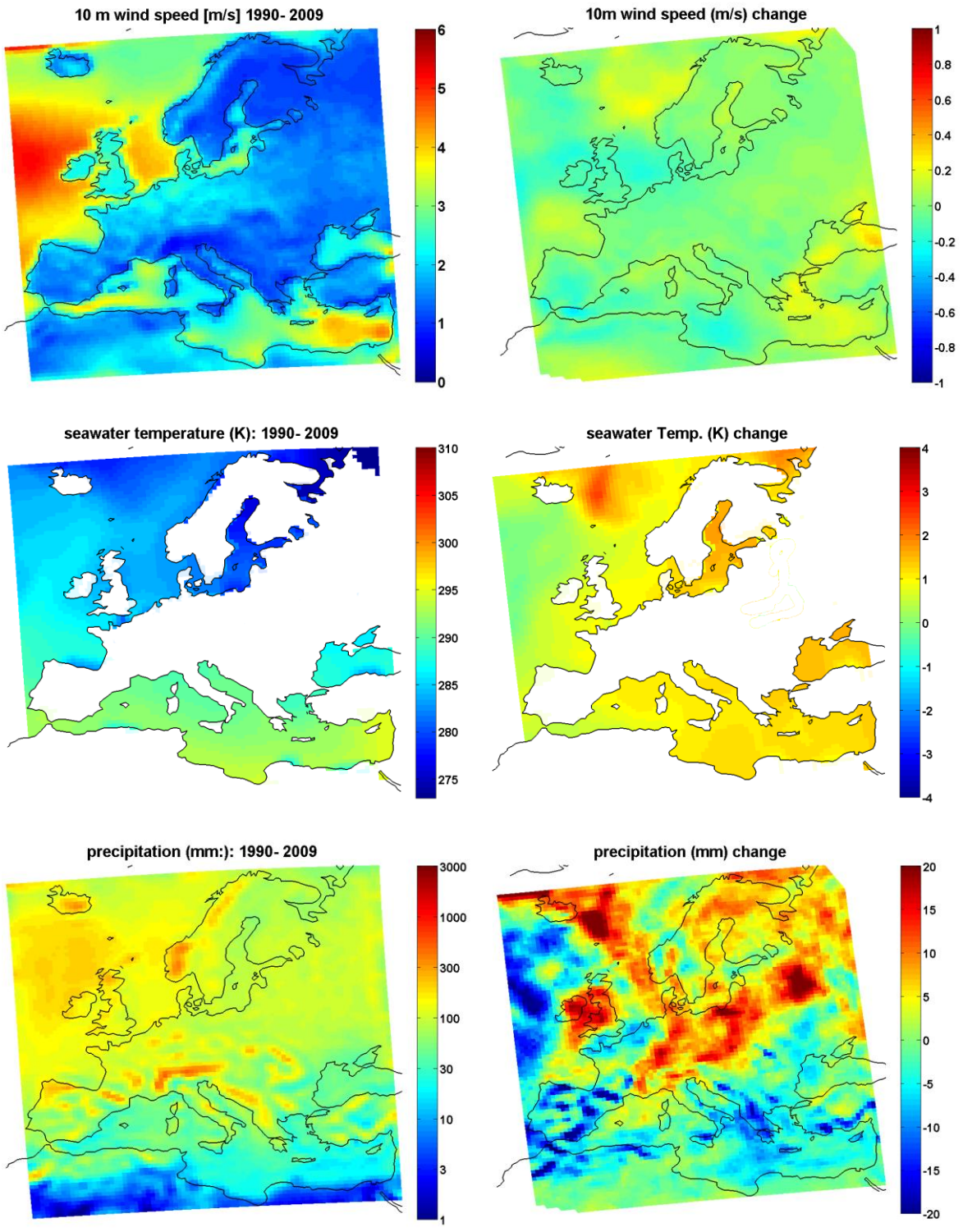

944

945 Figure 1. Top: Sea surface temperature (K), middle: wind speed (m s^{-1}), bottom: precipitation (mm). Left
946 panel: mean value for the past period (1990-2009); right panel: absolute difference between the future (2040-
947 2059) and past periods.

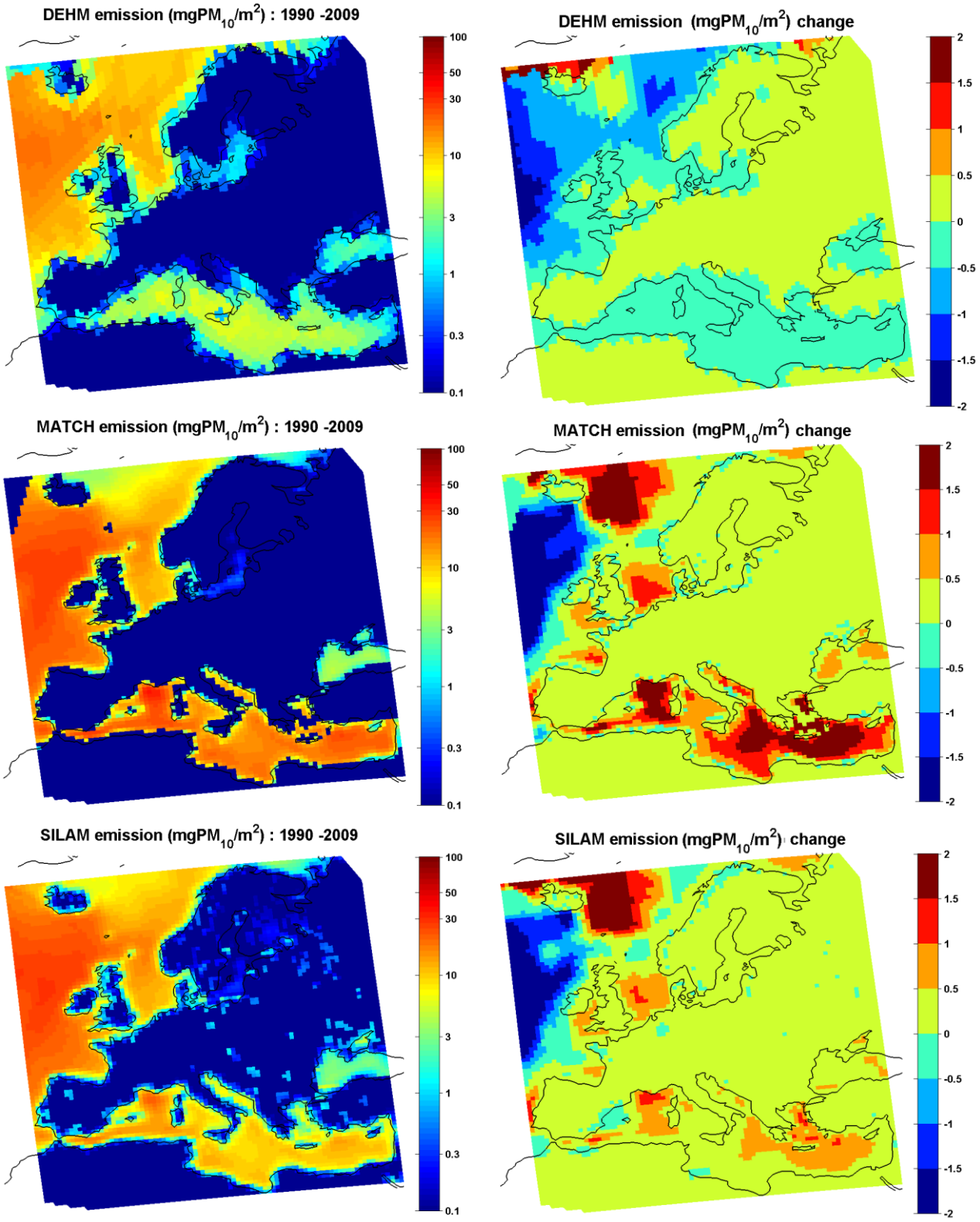

Figure 2. Annual sea salt emission ($mgPM_{10}\ m^{-2}$) for DEHM, MATCH and SILAM models. Left panel mean value for the past period (1990-2009); right panel: absolute difference between the future (2040-2059) and past periods.

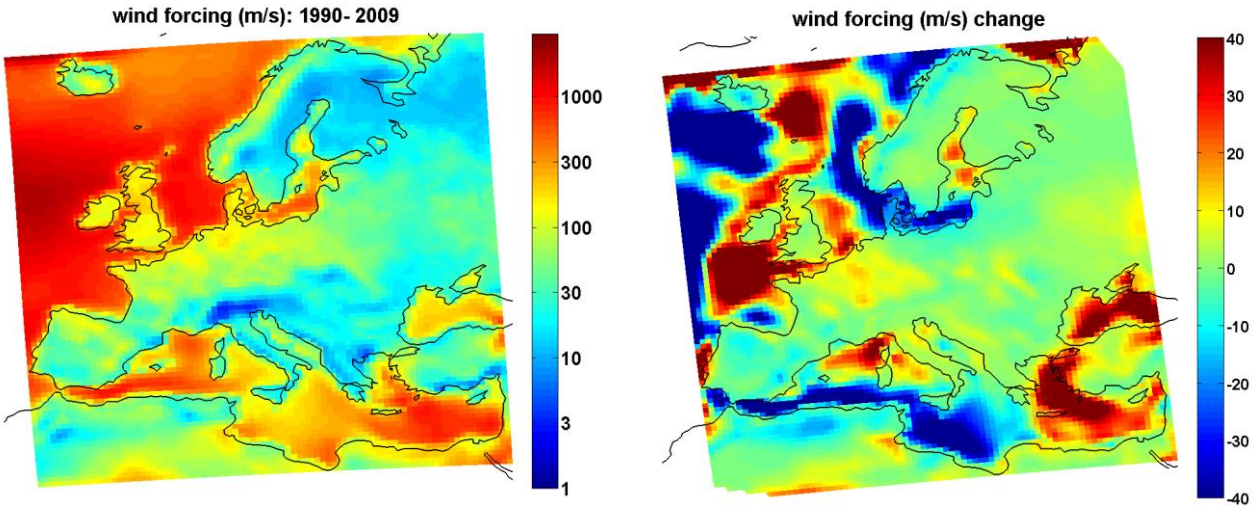

Figure 3. Wind forcing ($\approx U_{10}^{3.41}$). Left panel: past period (1990-2009); right panel: absolute difference between the future (2040-2059) and past periods.

1

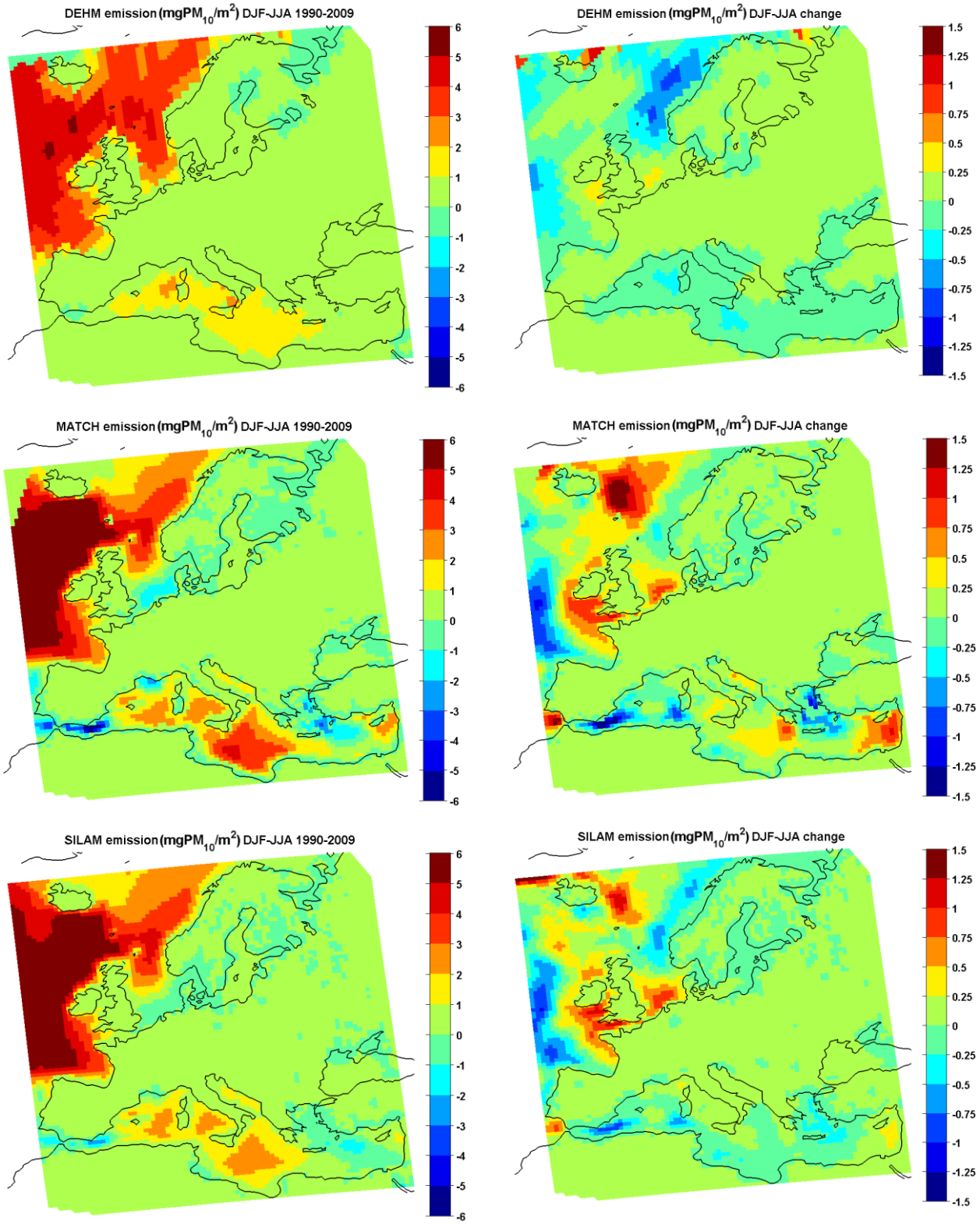

2 **Figure 4** Sea salt emission ($mgPM_{10}\ m^{-2}$) difference between winter (December, January and
3 February, DJF) and summer (June, July and August, JJA) for DEHM, MATCH and SILAM

models. Left panel: past period (1990-2009); right panel: absolute difference between the future (2040-2059) and past periods.

1

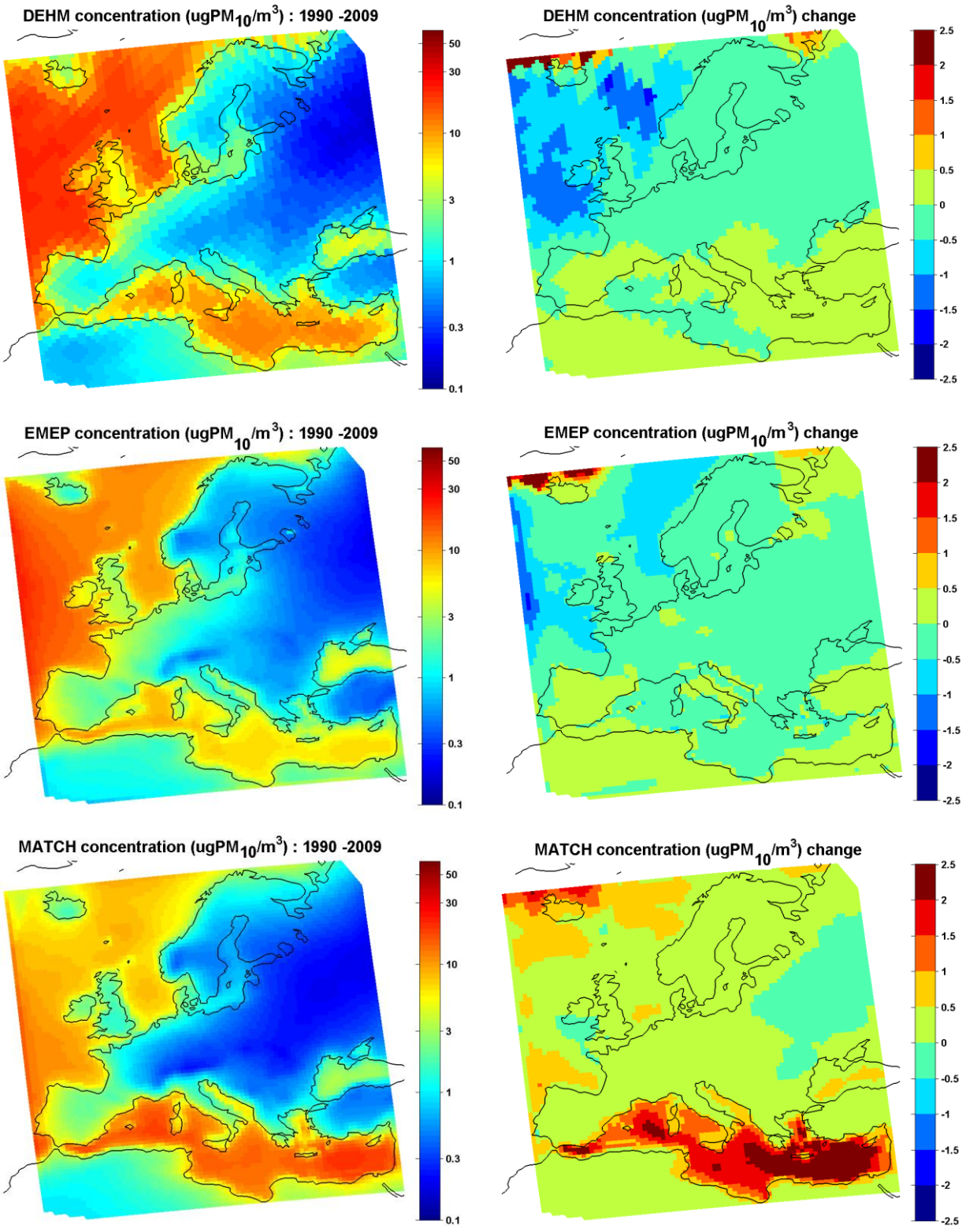
DEHM concentration (ugPM10/m3) : 1990 -2009
50
30
10
3
1
0.3
0.1
DEHM concentration (ugPM10/m3) change
2.5
2
1.5
1
0.5
0
-0.5
-1
-1.5
-2
-2.5
EMEP concentration (ugPM10/m3) : 1990 -2009
50
30
10
3
1
0.3
0.1
EMEP concentration (ugPM10/m3) change
2.5
2
1.5
1
0.5
0
-0.5
-1
-1.5
-2
-2.5
MATCH concentration (ugPM10/m3) : 1990 -2009
50
30
10
3
1
0.3
0.1
MATCH concentration (ugPM10/m3) change
2.5
2
1.5
1
0.5
0
-0.5
-1
-1.5
-2
-2.5

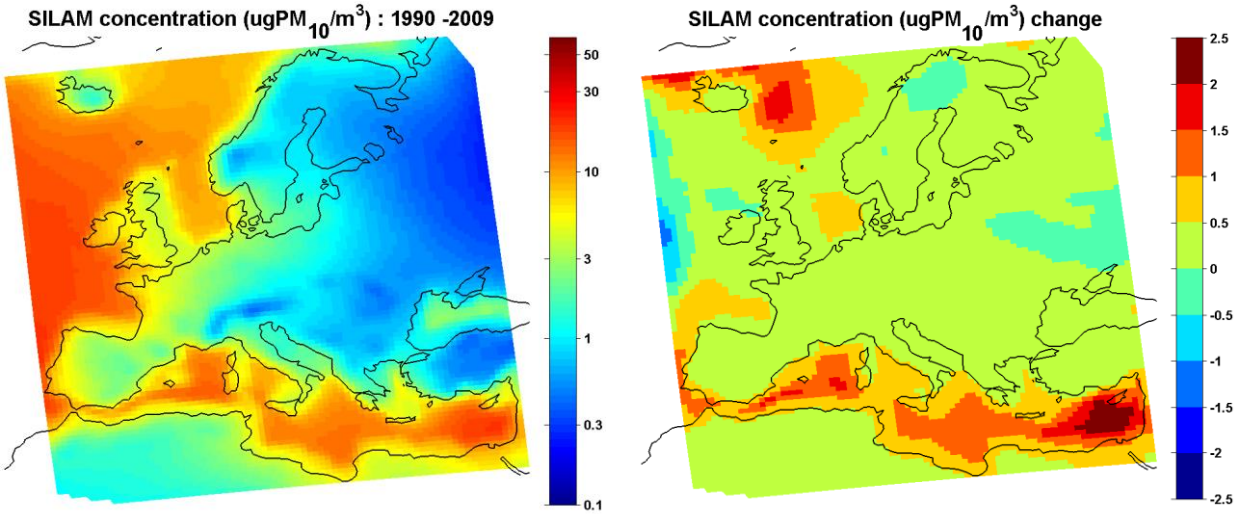

Figure 5. Sea salt surface concentration ($\mu gPM_{10}\ m^{-3}$) for DEHM, MATCH, EMEP and SILAM models. Left panel: mean value for the past period (1990-2009); right panel: absolute difference between the future (2040-2059) and past periods.

1

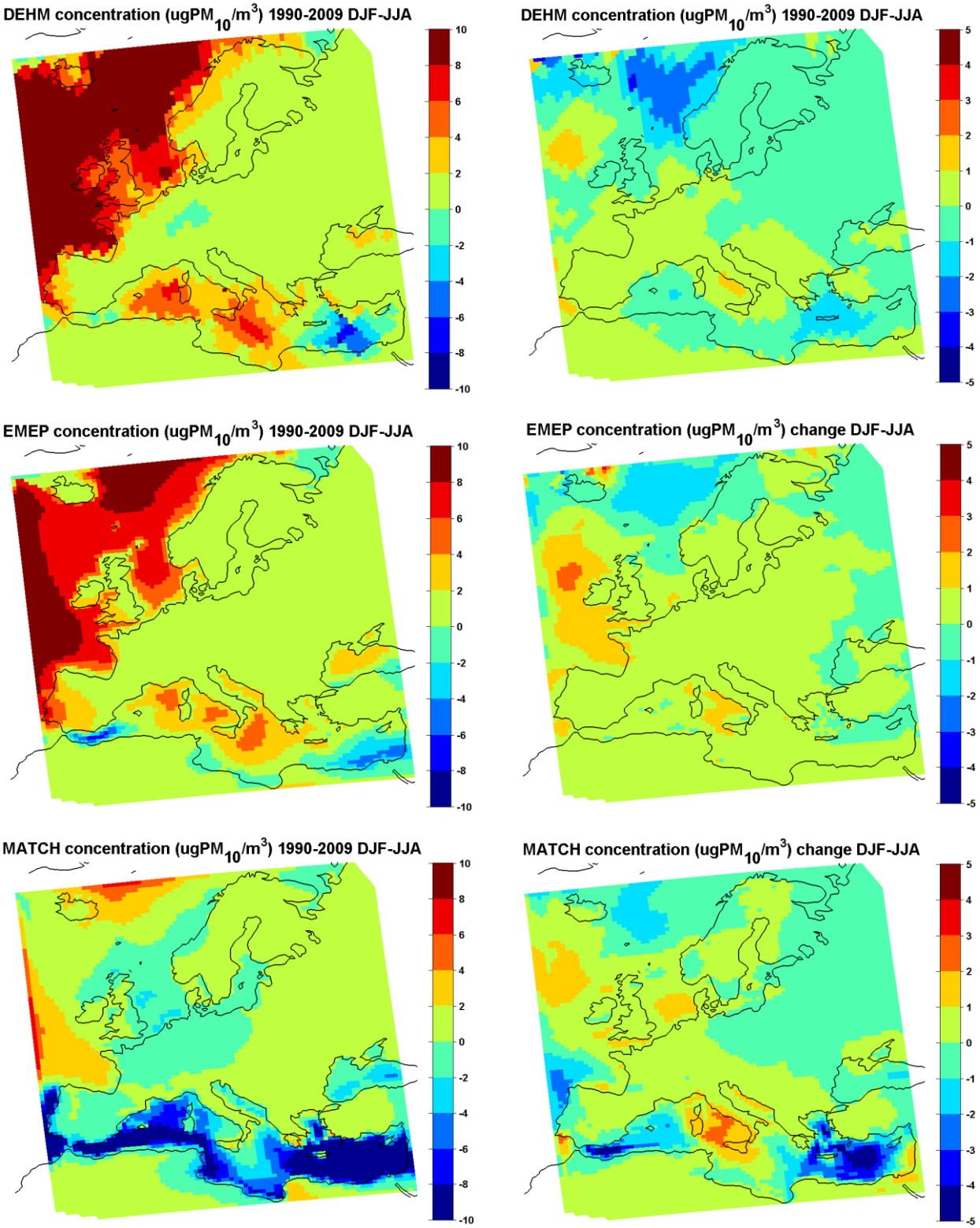
DEHM concentration (ugPM10/m3) 1990-2009 DJF-JJA
10
8
6
4
2
0
-2
-4
-6
-8
-10
DEHM concentration (ugPM10/m3) 1990-2009 DJF-JJA
5
4
3
2
1
0
-1
-2
-3
-4
-5
EMEP concentration (ugPM10/m3) 1990-2009 DJF-JJA
10
8
6
4
2
0
-2
-4
-6
-8
-10
EMEP concentration (ugPM10/m3) change DJF-JJA
5
4
3
2
1
0
-1
-2
-3
-4
-5
MATCH concentration (ugPM10/m3) 1990-2009 DJF-JJA
10
8
6
4
2
0
-2
-4
-6
-8
-10
MATCH concentration (ugPM10/m3) change DJF-JJA
5
4
3
2
1
0
-1
-2
-3
-4
-5

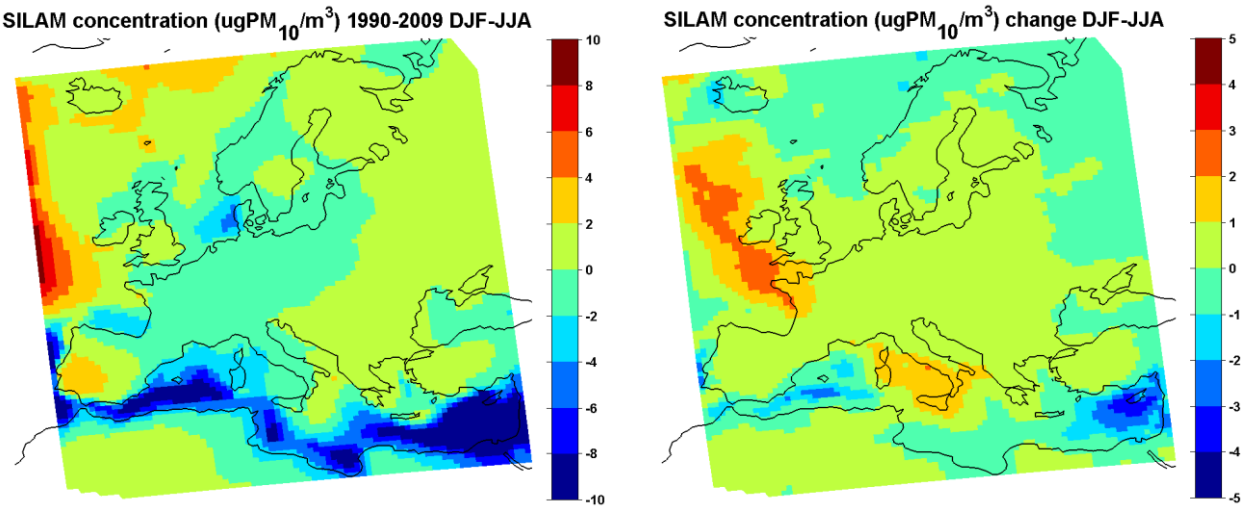

Figure 6 Sea salt concentration ($\mu gPM_{10}\ m^{-3}$) difference between winter (December, January and February, DJF) and summer (June, July and August, JJA) for DEHM, MATCH and SILAM models. Left panel: past period (1990-2009); right panel: absolute difference between the future (2040-2059) and past periods.

1

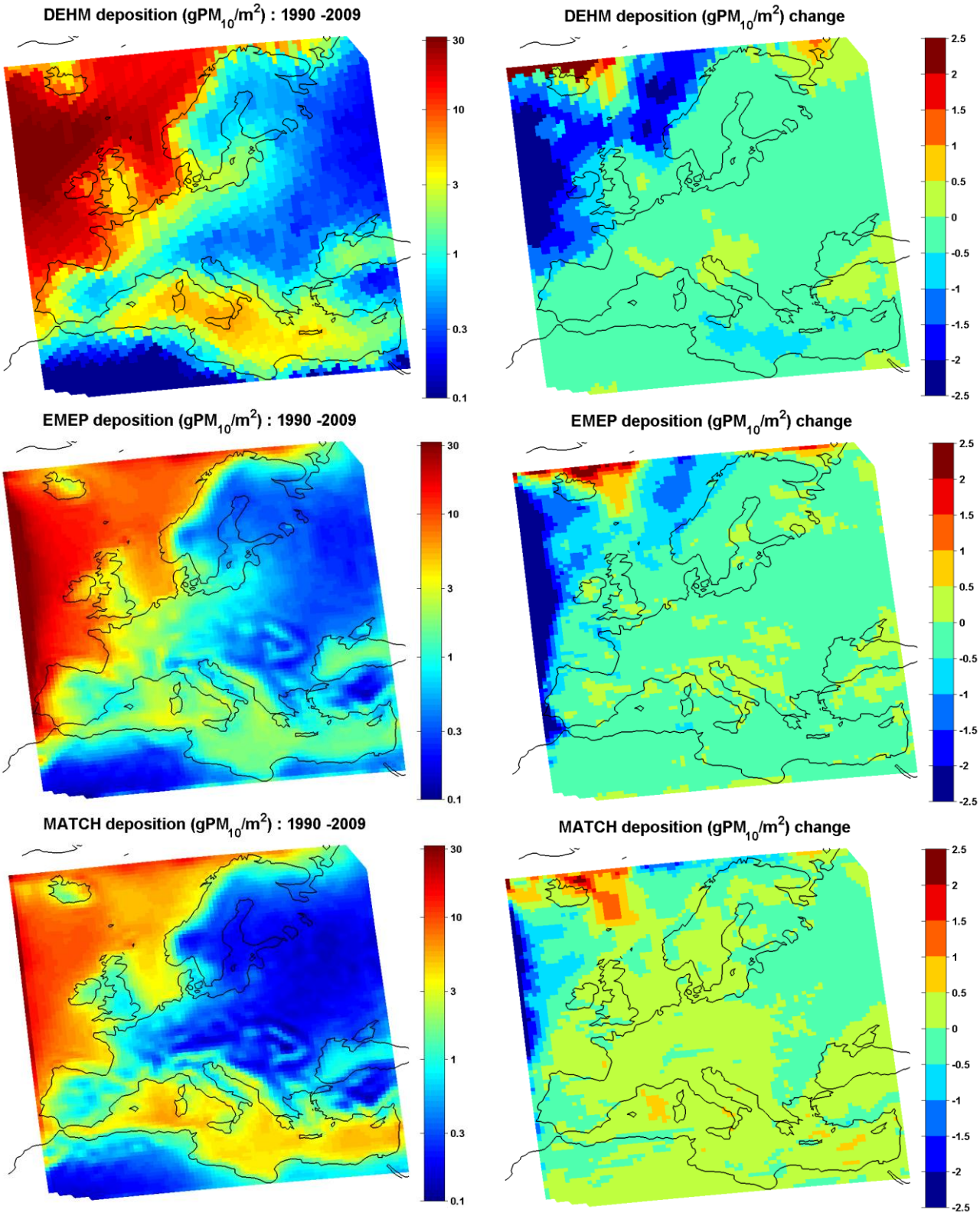
DEHM deposition (gPM10/m2) : 1990 -2009
30
10
3
1
0.3
0.1
DEHM deposition (gPM10/m2) change
2.5
2
1.5
1
0.5
0
-0.5
-1
-1.5
-2
-2.5
EMEP deposition (gPM10/m2) : 1990 -2009
EMEP deposition (gPM10/m2) change
MATCH deposition (gPM10/m2) : 1990 -2009
MATCH deposition (gPM10/m2) change

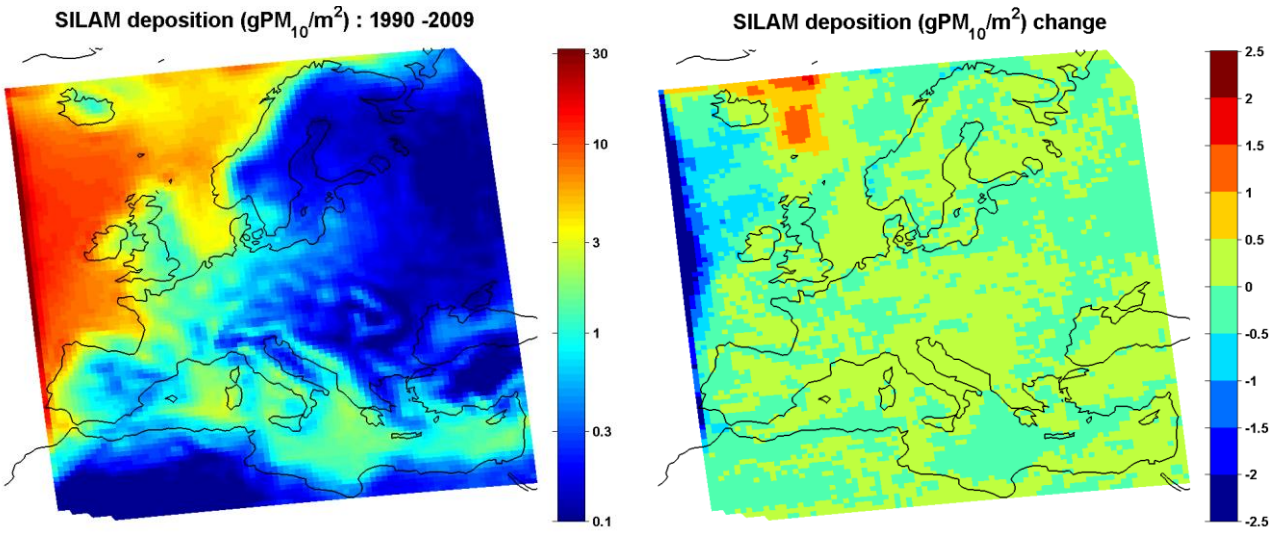

1

2 **Figure 7** Sea salt deposition (wet+dry) ($mgPM_{10}$ m^{-2}) for DEHM, MATCH, EMEP and
3 SILAM models. Left panel: mean value for the past period (1990-2009); right panel: absolute
4 difference between the future (2040-2059) and past periods.

5

1

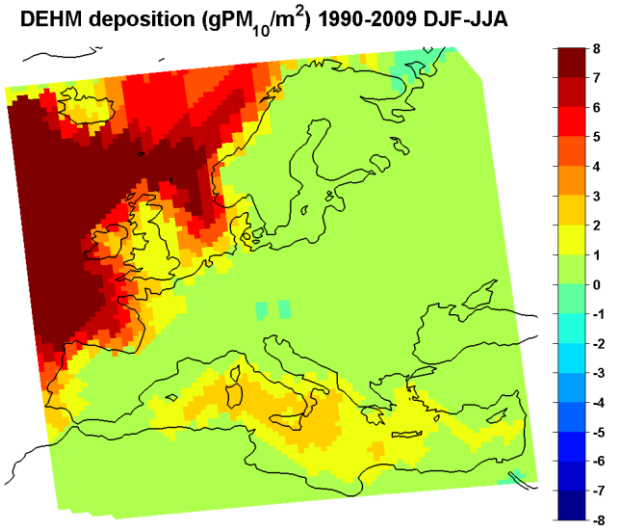
DEHM deposition (gPM10/m2) 1990-2009 DJF-JJA
8
7
6
5
4
3
2
1
0
-1
-2
-3
-4
-5
-6
-7
-8

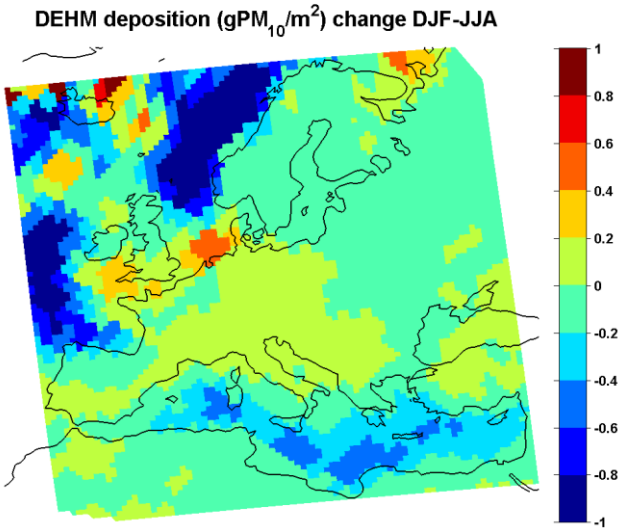
DEHM deposition (gPM10/m2) change DJF-JJA
1
0.8
0.6
0.4
0.2
0
-0.2
-0.4
-0.6
-0.8
-1

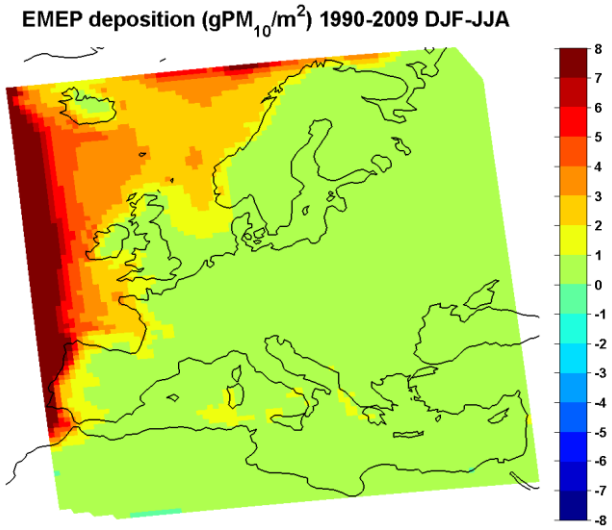
EMEP deposition (gPM10/m2) 1990-2009 DJF-JJA
8
7
6
5
4
3
2
1
0
-1
-2
-3
-4
-5
-6
-7
-8

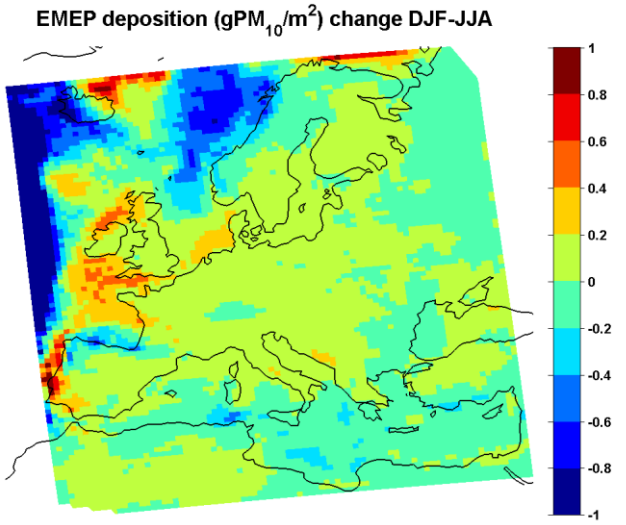
EMEP deposition (gPM10/m2) change DJF-JJA
1
0.8
0.6
0.4
0.2
0
-0.2
-0.4
-0.6
-0.8
-1

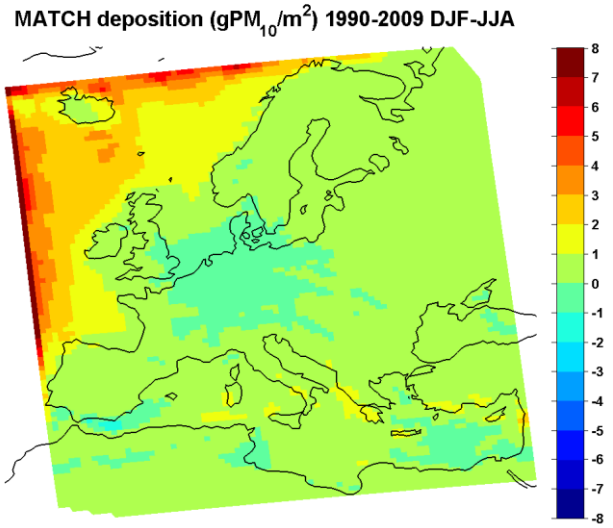
MATCH deposition (gPM10/m2) 1990-2009 DJF-JJA
8
7
6
5
4
3
2
1
0
-1
-2
-3
-4
-5
-6
-7
-8

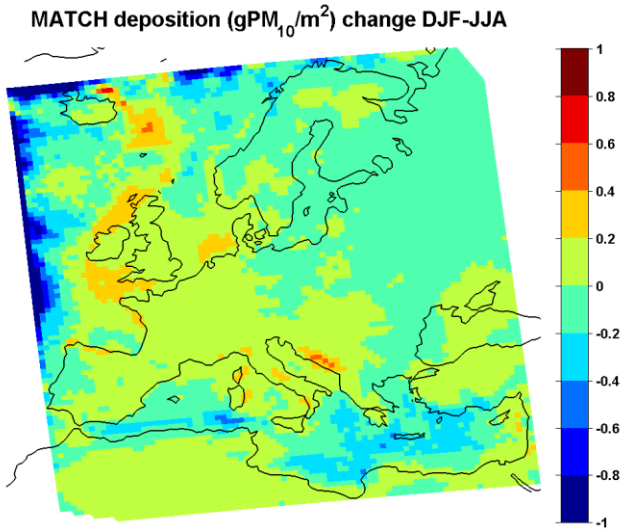
MATCH deposition (gPM10/m2) change DJF-JJA
1
0.8
0.6
0.4
0.2
0
-0.2
-0.4
-0.6
-0.8
-1

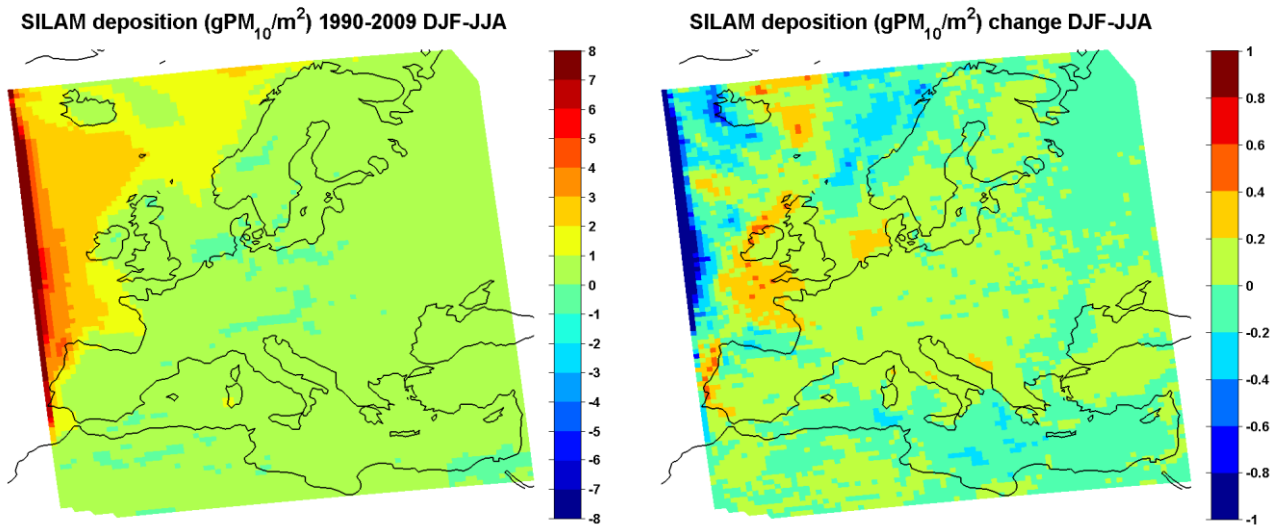

Figure 8 Sea salt annual deposition (gPM_{10} m^{-2}) difference between winter (December, January and February, DJF) and summer (June, July and August, JJA) for DEHM, MATCH and SILAM models. Left panel: past period (1990-2009); right panel: absolute difference between future (2040-2059) and past periods.

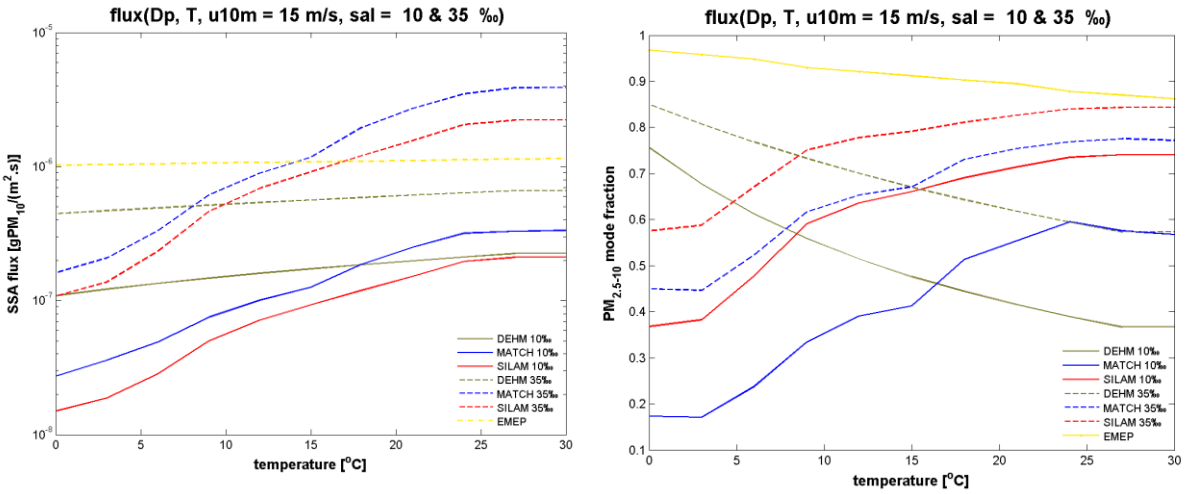

Figure 9. SSA mass flux (gPM_{10} m^{-2} s^{-1}) box calculations (left) and coarse mode fraction of the mass flux (right): as a function of radius (dry for DEHM and SILAM and RH = 80 % for MATCH) and temperature, for wind speed 15 m s^{-1} and salinities 10 ‰ and 35 ‰.

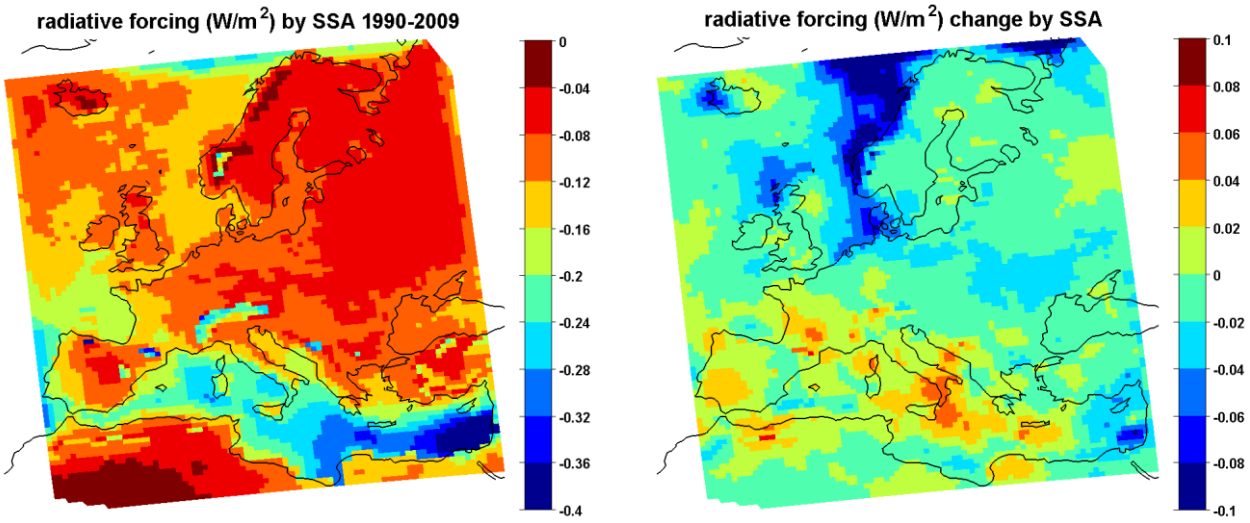

Figure 10. Radiative forcing by sea salt (W m^{-2}). Left panel: past period (1990-2009); right panel: absolute difference between future (2040-2059) and past periods.

1

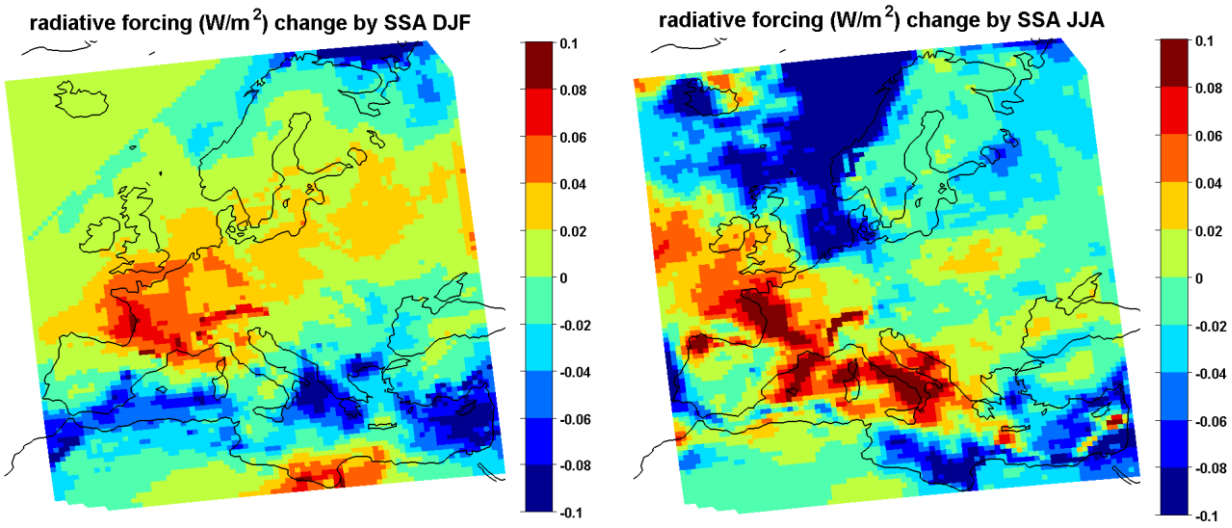

2

3 Figure 11. Radiative forcing by sea salt (W m^{-2}): difference between future (2040-2059) and
4 past periods. Left panel: winter (December, January and February); right panel: summer
5 (June, July and August)

6

7